THE MIRROR CHARGE EXCHANGE REACTION $^{13}C(^{13}N,^{13}C)^{13}N$

by

MATHIAS STEINER

A DISSERTATION

Submitted to
Michigan State University
in partial fulfilment of the requirements
for the Degree of

DOCTOR OF PHILOSOPHY

Department of Physics and Astronomy

1995

ABSTRACT

THE MIRROR CHARGE–EXCHANGE REACTION ^{13}C(^{13}N,^{13}C)^{13}N

By

Mathias Steiner

Differential cross sections have been measured near 0° for the dominant channels in the mirror reaction ^{13}C(^{13}N,^{13}C)^{13}N at E/A = 57 and 105 MeV. The cross sections of the peaks in the excitation spectrum are discussed in terms of the Gamow–Teller and Fermi transition strengths in the target and the projectile. The cross section per unit Gamow–Teller strength is found to be enhanced relative to that for unit Fermi strength when compared with previous results from (p,n) reactions. The use of heavy ions as probes for weak–interaction strengths in radioactive nuclei is disussed.

The present work represents the first use of mirror symmetry to study heavy–ion charge exchange as well as the first application of the developing radioactive nuclear beam field to this area.

Meinen Eltern gewidmet

ACKNOWLEDGEMENTS

Before I start to thank those individuals who have made a difference during the last four years, I want to thank Michigan State University, the NSCL, and the National Science Foundation for providing support and the opportunity to do my Ph.D. work in this country.

When I first arrived at the Cyclotron, I was hoping to be able to work for Brad Sherrill, who had been warmly recommended to me by several physicists at GSI in Darmstadt, Germany. In retrospect, he really didn't get much of a chance to say no... Brad gave me plenty of freedom in my work, but he was always there to help, advise, or console as needed. Not to mention the fact that it was he who really got the charge–exchange experiments off the ground. Thank you for being a great boss!

Speaking of bosses, Dave Morrissey was very supportive throughout. Be it postscript problems, nuclear electronics, or the recalibration of the beamline magnets, Dave would always help out. His help as well as his, ah, frank conversational style are very much appreciated.

There is no better tonic for a young physicist's frayed nerves than a chat with Walt Benenson, nuclear experimentalist extraordinaire and elder statesman of the A1200 group.

Thanks are also due to those who contributed to my thesis experiments: Ed, Nigel, Bob, Mike, Sherry, and Brian in the first test run, and later on Daniel, Jim, Mikey, Maggie, Ned, Toshiyuki, Raman, and Chris. Everything had to work just so for the charge–exchange runs, and (almost) everything did. Thanks a lot, folks!

Many thanks also to the cyclotron support staff, which is truly deserving of its name. Thanks to Jeff for a great tuning job, and to Tim for a ton of beam.

The original idea for the mirror charge–exchange experiments came from George Bertsch, for which I am grateful. As far as the theory behind the experiments is concerned, I was pretty much in the dark for a considerable length of time. I want to thank Sam Austin, Carlos Bertulani, Alex Brown, Scott Pratt, Jack Rapaport, and John Watson for helpful discussions on charge exchange. Anantaraman and Jim Carr helped me understand the double–folding model.

Without any doubt, those who shared an office with me deserve special mention: Don, my choice for "best tantrum", and Brian, who inflicted his infernal radio programs on the rest of us. Oh well. Ever since Brian left, things have gotten a lot quieter (except when "Car Talk" is on). It has further been my pleasure to share the office with Sally and Jing, and with Mikey (as long as he doesn't explain how "life stinks", and why).

Further thanks are due to Ron, Jac, Thomas, and Renan for three great DALMAC tours; to Michael T. for a memorable teaching experience; to Phil, for culinary and cultural support; to Jon, for his unwavering support in times of need (love machine breakdown); to Damian, for comic relief; and to Dave, Nancy, and Michael for a glimpse of what it's like.

This work was made possible, in part, by the Peanut Barrel, El Azteco, Velocipede Peddler, Meridian Auto Parts, and the Sears tool department. Without these fine establishments, life would not have been the same.

Finally, I want to thank Charlotte for always being there for me.

Contents

Chapter 1

Introduction

Recent developments in the rapidly growing field of radioactive nuclear beams (RNB) have opened up new areas of research, and RNBs can be expected to help answer a number of important questions in nuclear physics. Experiments with a wide variety of radioactive nuclei, many of them of astrophysical importance, have become possible and exciting new phenomena are being observed. For example, halo nuclei are currently among the most intensely studied objects in nuclear–structure physics [Rii94]. Radioactive beams also make available nuclei with special symmetries such as doubly magic ^{100}Sn [LeA94, ScF94].

One new capability provided by RNBs are nuclear reaction studies with pairs of mirror nuclei, since only one member of a mirror pair can be stable and a radioactive beam is necessary to provide the partner of the stable target nucleus. Due to their special symmetry, mirror pairs are a useful tool for the study of the strong force in a nuclear environment and provide a unique opportunity for attaining the long–term goal of understanding charge exchange in heavy ions. In this work, the relative importance of spin–flip and non–spin–flip contributions in heavy–ion charge exchange (HICEX) is investigated, and the usefulness of the reaction as a method of determining Gamow–Teller (GT) transition strengths in nuclei is explored.

Weak–interaction strengths are of fundamental interest for our understanding of the nucleus, and GT matrix elements for a large number of radioactive nuclei are important parameters in nuclear astrophysics. The physics and terminology of charge–exchange reactions are introduced in chapter 2. A large part of this chapter is devoted to the (p,n) reaction, which constitutes the majority of charge–exchange work done to date. It has been established over the course of the last 15 years that the zero–degree (p,n) cross sections observed for a given target nucleus are closely proportional to the corresponding weak–interaction transition strengths, a phenomenon labelled "specific proportionality." Heavy–ion charge exchange is presented in the same framework, and the differences to nucleon–induced CEX reactions are discussed. Relatively few HICEX experiments have been performed to date, and the work described here is the first such study using radioactive beams as well as the first nuclear reaction performed with a pair of mirror nuclei.

Due to the relatively poor emittance of the secondary beam, these experiments are difficult to perform, and it is one of the goals of this study to investigate the general feasibility of high–resolution nuclear–structure experiments with radioactive beams. Chapter 3 describes how this was achieved. Detailed experimental parameters are given, and considerable space is devoted to the ion–optical conditioning in the A1200 fragment separator. Ion optics is a topic of increasing importance in RNB physics, but concrete experimental examples are still scarce in the literature.

In chapter 4, the analysis of the data is described in detail, and the interpretation of the spectra is discussed. The final results are presented in chapter 5 and compared to other charge–exchange results.

The ^{13}C(^{13}N,^{13}C)^{13}N energy spectra are easily interpreted in terms of weak–interaction transitions in both the target and the projectile. Other amplitudes ap-

pear to be of little importance at forward angles. The symmetry of the mirror pair greatly aids in analysing the data and allows the extraction of the so–called Fermi and Gamow–Teller "unit cross sections", in close analogy to the parameters used in (p,n) work. Mirror symmetry further aids in extracting the relative strength of Fermi and GT contributions from the data. The unit cross sections observed in the present work are found to be significantly larger than other HICEX results, which illustrates the need to carefully calibrate the relationship between yield and GT matrix elements. A controversy regarding the exact values of the transition strengths in ^{13}C prevents a rigorous quantitative analysis at this time, but the observed cross sections are fully compatible with the assumption of specific proportionality.

Even though some difficulties still persist in the precise understanding of the underlying physical processes, the results of the present experiments indicate that heavy–ion charge exchange has the potential to become a powerful tool for GT strength measurements in radioactive nuclei.

Chapter 2

Charge–Exchange Reactions

Charge–exchange reactions play an important role in our current understanding of the nuclear force. This is illustrated by the two–nucleon system. Only one of the three possible systems — the deuteron – is bound, but neither the dineutron nor the diproton is. While the similarity of the n–n and p–p systems established the approximate charge–indipendence of the nuclear force, deuteron binding provided an indicator of the spin–dependence of the nuclear force. Most of the detailed information on the nucleon–nucleon interaction, however, was obtained through scattering experiments. One of the most important and interesting results is shown in Fig. 2.2, which shows the angular distribution of the ^{1}H(n,p)n reaction at an incident neutron energy of 200 MeV. While the peak at forward angles (0°) is a general feature of elastic scattering from a potential, the sharp peak at backward angles (180°) is evidence for 0° (n,p) charge–exchange scattering, as shown schematically in Fig. 2.1. Together with data from (p,p) and (n,n) scattering experiments over a wide range of energies, the charge–exchange results led to the formulation of the one–pion exchange potential [dSF74]:

$$V_{\mathrm{OPEP}} = \frac{1}{3}\frac{g^2}{\hbar c} m_\pi c^2 (\tau_1 \cdot \tau_2) \left[(\sigma_1 \cdot \sigma_2) + \left(1 + \frac{3}{\mu r} + \frac{3}{(\mu r)^2} \right) S_{12} \right] \frac{e^{-\mu r}}{\mu r}, \qquad (2.1)$$

Figure 2.1: [dSF74] Schematic description of charge–exchange scattering; scattering of the original proton through the angle θ looks like backward scattering by an angle $\pi - \theta$ if charge is exchanged.

where σ and τ are the spin and isospin operators, respectively, S_{12} is the tensor operator,

$$S_{12} = \frac{1}{r^2}\left[3(\sigma_1 \cdot \mathbf{r})(\sigma_2 \cdot \mathbf{r}) - (\sigma_1 \cdot \sigma_2)\right], \tag{2.2}$$

and $g^2/\hbar c$ is a coupling constant. Equation 2.1 provides the link to weak–interaction physics, as it contains the $< \sigma\,\tau >$ operator. The importance of charge–exchange reactions for measurements of β–decay transition strengths is discussed in the next section.

Surprisingly, despite the myriad of nuclear reaction experiments performed over the past half–century, the ^{1}H(n,p)n reaction remains the only scattering experiment with a mirror system to date. The reason for this is the fact that only one member of a mirror pair can be stable and that a radioactive beam or target is therefore necessary to perform these experiments. The increasing availability of radioactive beams finally made mirror charge exchange a possibility. While nucleon–nucleon scattering is one of the most basic tools of probing the nuclear force, charge exchange with "real" mirror nuclei presents a much more intricate problem. Some of the complications arising from the extended nature of the projectile will be addressed in section 2.4.

The special symmetry of the mirror pair greatly aids in analysing and interpret-

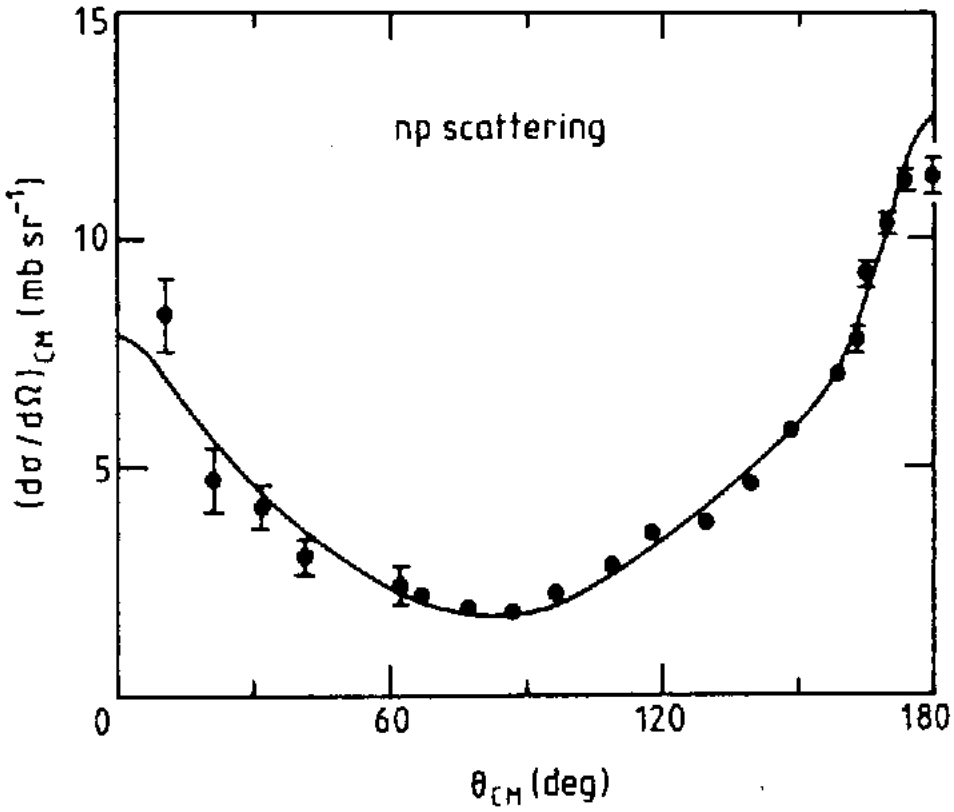

Figure 2.2: [BeE87] Angular distribution of elastic (n,p) scattering at 200 MeV. The curve is calculated from phase shifts. Note the sharp peak at 180° scattering.

ing the resulting spectra and extracting information on the underlying physics of the charge–exchange process. Furthermore, the zero Q value of the mirror reaction ensures that the transition densities will be probed over the entire range of momentum transfer including the important region around q = 0.

The goals of this study are to learn more about the mechanisms of heavy–ion charge exchange and to investigate the feasibility of using these reactions to measure weak–interaction strengths in radioactive nuclei. The strength and location of Gamow–Teller resonances in many fp–shell nuclei are important and highly sensitive parameters in astrophysical calculations describing the evolution of type II supernova progenitors [AuS93]. Measurements of GT strengths in radioactive nuclei in the iron region are very difficult with presently available methods, and charge–exchange reactions with radioactive nuclei have the potential to become powerful tools for determination of these parameters. Finding workable experimental solutions to this problem is all the more important because shell–model calculations in this mass region have been shown to be unreliable [AuS93].

2.1 The (p,n) Reaction

Over the past 15 years, nucleon–induced charge–exchange reactions have received much attention. The discovery of both the isobaric–analog state [AnW61] and the Gamow–Teller resonance [DoG75] were achieved using (p,n) charge–exchange scattering. Perhaps the most important application of the (p,n) reaction in the energy regime of 100 MeV and above is the measurement of GT strengths in nuclei for excitation–energy regions that are inaccessible to β–decay. A close correspondence between zero–degree (p,n) cross section and β–decay transition strength has been found [GoG80] and has been thoroughly investigated. A short summary of these re-

sults will be given in the following. For comprehensive reviews, the reader is directed to Refs. [TaG87, BeE87].

Proportionality between β–decay transition strengths and (p,n) cross sections is supported by standard reaction theory as well as experimental observation. The correspondence is due to the similarity of the operators involved in each type of reaction. The central isovector terms in the effective nucleon–nucleon interaction that mediate low momentum–transfer spin–flip ($\Delta S = 1$) transitions,

$$\sum_i V_{\sigma\tau}(r_{ip})\sigma_{\mathbf{i}} \cdot \sigma_{\mathbf{p}}\, \tau_{\mathbf{i}} \cdot \tau_{\mathbf{p}}, \tag{2.3}$$

and non–spin–flip ($\Delta S = 0$) transitions,

$$\sum_i V_{\tau}(r_{ip})\tau_{\mathbf{i}} \cdot \tau_{\mathbf{p}}, \tag{2.4}$$

are similar to the corresponding operators

$$G_A \sum_i \sigma_i t_i^{\pm} \text{ and } G_V \sum_i t_i^{\pm} \tag{2.5}$$

for Gamow–Teller and Fermi β–decay, respectively [TaG87]. The sum is over target nucleons, and the index p indicates the projectile.

The model that is most commonly used to describe the (p,n) reaction is the distorted–wave impulse approximation (DWIA). It factorizes the process into a nuclear–structure and a nuclear–reactions part and employs the free nucleon–nucleon interaction for the charge–exchange mechanism itself. At zero momentum transfer, the DWIA cross section for a mixed Fermi or GT transition is of the form [TaG87]:

$$\frac{d\sigma}{d\Omega}(0^o) = \left(\frac{\mu}{\hbar^2\pi}\right)^2 \frac{k_f}{k_i}\left(N_{\sigma\tau}^D\,|J_{\sigma\tau}|^2\,B(GT) + N_{\tau}^D\,|J_{\tau}|^2\,B(F)\right), \tag{2.6}$$

where μ is the reduced mass and k_i and k_f are the initial and final wave vectors of the incident nucleon. J is the volume integral of the interaction strength and has units

of MeV fm^3. The distortion factor N^D is a number that accounts for the distortion of the incoming plane waves by the nuclear potential. It is given by the ratio of cross sections calculated for plane waves and waves distorted by an optical potential:

$$N^D = \left. \frac{d\sigma(DW)/d\Omega}{d\sigma(PW)/d\Omega} \right|_{\theta=0^\circ} \tag{2.7}$$

and can be calculated reliably in DWIA, i.e. with little dependence on the details of the model.

An simplified, empirical form of Eq. 1.7 is most useful for comparisons of experimental results:

$$\sigma = \hat{\sigma}_\alpha(E_p, A) F_\alpha(q, \omega)\, B(\alpha), \tag{2.8}$$

where α = F or GT and σ denotes the forward cross section at 0°. The proportionality constant $\hat{\sigma}$ is called the "unit cross section" and can be dependent on the target mass and the bombarding energy. The effect of a non–zero Q value is taken into account through the factor $F(q, \omega)$, which describes the shape of the cross section distribution as a function of momentum transfer q and energy loss ω [1] and goes to unity as q and ω go to zero. This factor can be calculated in reaction theory, and for small values of q and ω, simple parametrizations have been shown to describe the experimental data well without reliance on particular models [TaG87]

The factor $\hat{\sigma}$ has been the subject of extensive empirical studies [GoG80, TaG87, RaW87]. The relationship between (p,n) cross section and β–decay for different transitions starting from the same parent state is commonly referred to as "specific proportionality", while the term "general proportionality" describes comparisons of cross sections for transitions originating from different target nuclei. Specific proportionality is fulfilled for the majority of nuclei, and once $\hat{\sigma}$ has been determined from transitions with known β–decay strength, (p,n) cross sections can be used with

[1] ω describes the effects of excitation energy: $\omega = E_x - Q_{gs}$, where Q_{gs} is the Q value for the reaction to the ground state.

confidence in most cases to determine the unknown B(GT) values. However, there is no smooth target dependence, and proportionality constants inferred or extrapolated from different target nuclei have to be regarded as uncertain at the 20% to 50% level [TaG87].

Another problem that up to now has not been solved is the phenomenon known as quenching of GT strength. This refers to the fact that the summed GT strength, as observed in the (p,n) reaction and normalized to known β–decay measurements, falls approximately 40% short of the predicted total GT strength. This behaviour has been observed for a wide range of nuclei and appears to be universal.

The total Fermi strength is concentrated in the transition to the isobaric analog state and is easily calculated as $\mathrm{B(F)} = \mathrm{N} - \mathrm{Z}$. In contrast to this, the Gamow–Teller strength is fragmented over a number of nuclear states, and the corresponding sum rule is less rigorous:

$$\mathrm{B(GT)}_{\beta-} - \mathrm{B(GT)}_{\beta+} = 3(\mathrm{N} - \mathrm{Z}). \tag{2.9}$$

This only fixes the difference in total strength for β^- and β^+ decay, but since the β^+ strength function is quite weak, the sum rule can be viewed as a close lower bound on the β^- strength and is called the sum–rule bound. In n decay, for example, $\mathrm{B(GT)} = 3$ is indeed observed. The quenching of Gamow–Teller strength is illustrated in Fig. 2.3, which shows a comparison between GT amplitudes obtained from shell–model calculations and those measured from β–decay.

While β–decay is limited to a small energy range and permits comparison to theory only for selected transitions, the (p,n) reaction covers tens of MeV of excitation energy and allows comparison of individual transitions as well as overall integrated GT strength. Fig. 2.4 illustrates the experimental situation: The fraction of the sum–rule bound observed in (p,n) reactions at intermediate energies is plotted for a

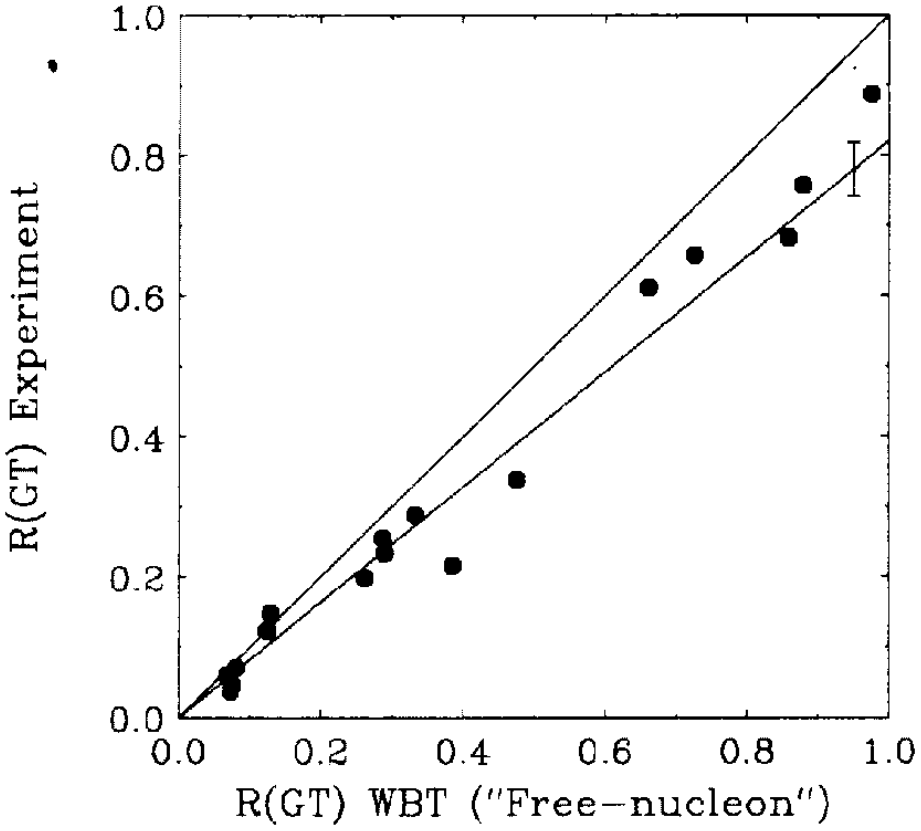

Figure 2.3: [ChB93] Comparison of GT matrix elements for sd–shell nuclei with the predictions from a shell–model Hamiltonian [?]. The matrix elements are normalized so that 1 corresponds to the maximum permitted by the shell model space. For perfect agreement, the points should lie on the diagonal line. They actually cluster around a line with a slope of 0.77, showing the quenching of GT strength. Note that this corresponds to a B(GT) quenching factor of $0.77^2 = 0.59$.

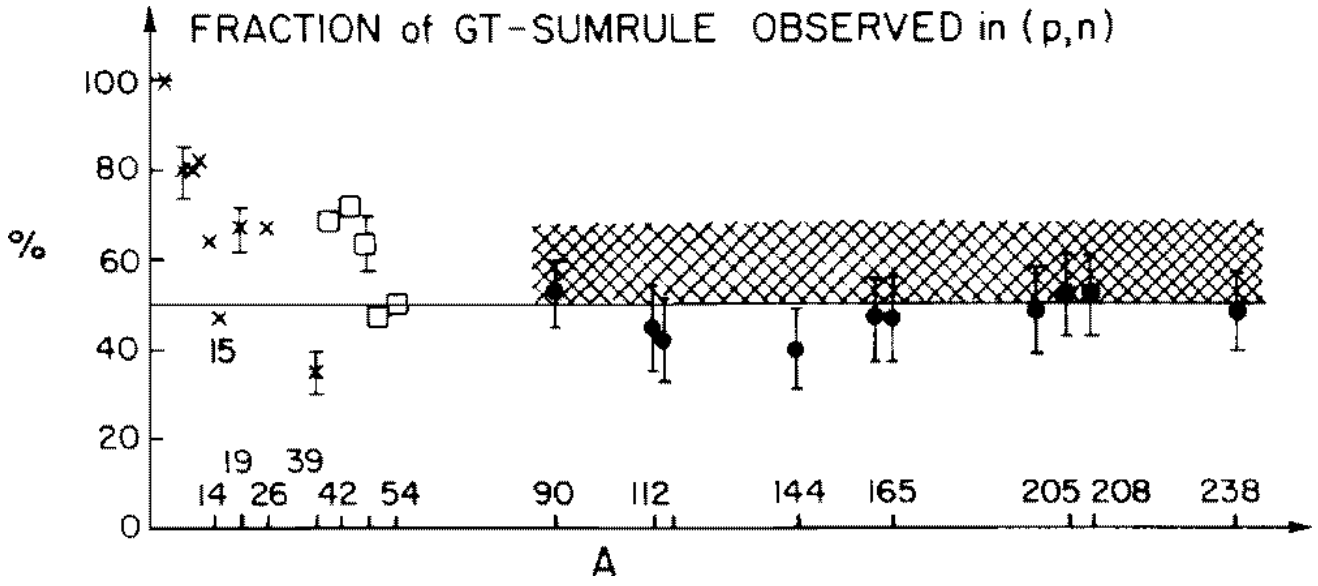

Figure 2.4: [Gaa85] Percent of sum rule bound observed by integrated (p,n) cross section for a variety of targets.

variety of targets [Gaa85]. The difference between the cross–hatched area and the full data points is due to the difficulty of resolving individual peaks for heavy targets. The transition from 100% of the sum rule bound observed in the ^{1}H(n,p)n case to 60% quenching for heavier nuclei is remarkably smooth and invites speculation that the quenching is an in–medium effect that reaches saturation around A = 20.

Subnuclear degrees of freedom, such as pions and the delta isobar excitation, may act to quench the strength in the spectroscopic region. Another possible explanation is configuration mixing, which may act to shift the strength to much higher energies, where experimental observation would be very difficult. be very difficult.

2.2 Fermi and GT Transitions

Transitions with $\Delta S = 0$ are analogous to Fermi β–decay, and the transition to the isobaric analog state (IAS) is proportional to the Fermi transition strength $B(F) = N - Z$, where N and Z are the neutron and proton number of the target residue. Since B(F) is easily calculated and concentrated on one single state, the value of $\hat{\sigma}_F$ can usually be determined with ease. If a relationship between $\hat{\sigma}_F$ and $\hat{\sigma}_{GT}$ can be found, the IAS (p,n) cross section can be used to calibrate the unit cross sections. This works especially well for 0^+ to 0^+ transitions, which are purely Fermi in nature. Fig. 2.5 shows the 0^o ^{14}C(p,n)^{14}N cross sections at incident proton energies between 80 and 650 MeV. The spectra have been normalized to the strength of the 1^+ GT peak, and the dashed line indicates the relative strength of the 0^o IAS peak. The ratio of Gamow–Teller to Fermi unit cross section can be parametrized as

$$\frac{\hat{\sigma}_{GT}(E_p,\, A)}{\hat{\sigma}_F(E_p,\, A)} = [R(E_p,\, A)]^2, \tag{2.10}$$

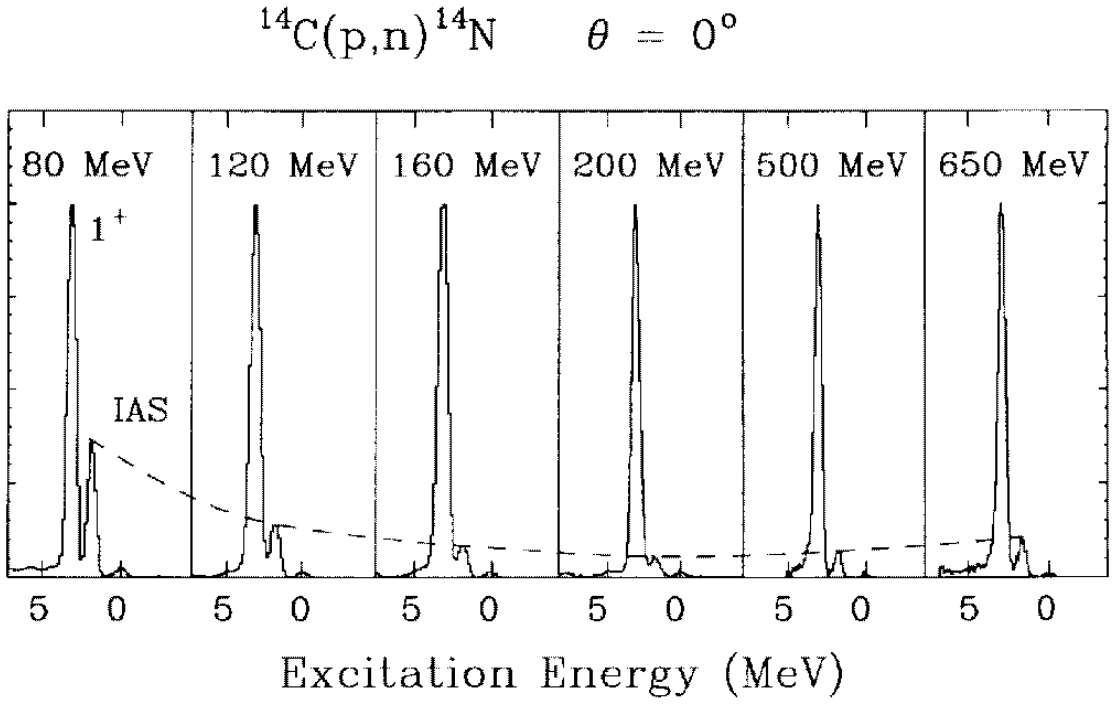

Figure 2.5: [RaS95] Zero–degree cross–section spectra for the ^{14}C(p,n)^{14}N reaction at the indicated bombarding energies. The spectra have been normalized arbitrarily.

and may be interpreted as the ratio

$$R^2 \simeq \frac{|J_{\sigma\tau}|^2}{|J_\sigma|^2}\frac{N^D_{\sigma\tau}}{N^D_\tau}, \tag{2.11}$$

as introduced in Eqs. 2.6 and 2.7. Between energies of approximately 20 and 200 MeV, the following parametrization yields good results:

$$R(E_p) = \frac{E_p}{E_0}, \tag{2.12}$$

with $E_0 = 55.0 \pm 0.4$ MeV, with little or no A–dependence observed. This relationship is illustrated in Fig. 2.6, where the value of R^2 is plotted versus the incident proton energy for a variety of even–A and odd–A targets. Aside from the lowest–energy data, the agreement between the data and the empirical relationship is excellent. In this energy region, the change in relative strength is due to a decrease of $\hat{\sigma}_F$ with increasing energy, while $\hat{\sigma}_{GT}$ stays approximately constant [BeE87].

2.3 The ^{13}C Controversy

Knowing the relative strengths of Fermi and GT cross sections is especially important for transitions that can have either $\Delta S = 0$ or $\Delta S = 1$, such as the transition to the ground state in the ^{13}C(p,n)^{13}N reaction. The J^π of the initial and final state is $\frac{1}{2}^-$, and the reaction can take place either via the Fermi or the Gamow–Teller interaction. The corresponding cross section then contains both contributions, which cannot be disentangled without relying on further information. If Eq. 2.7 holds, knowledge of B(F) and B(GT) may be used to extract the values of $\hat{\sigma}$. However, there are some cases, most notably the odd–A nuclei ^{13}C and ^{15}N, where the assumptions of specific proportionality have been called into question. Fig. 2.7 shows the excitation spectrum of the ^{13}C(p,n)^{13}N reaction at $E_p = 120$ MeV. For the ground state and the excited state at 15.1 MeV, which is the isobaric analog of the ^{13}B ground state, GT strengths

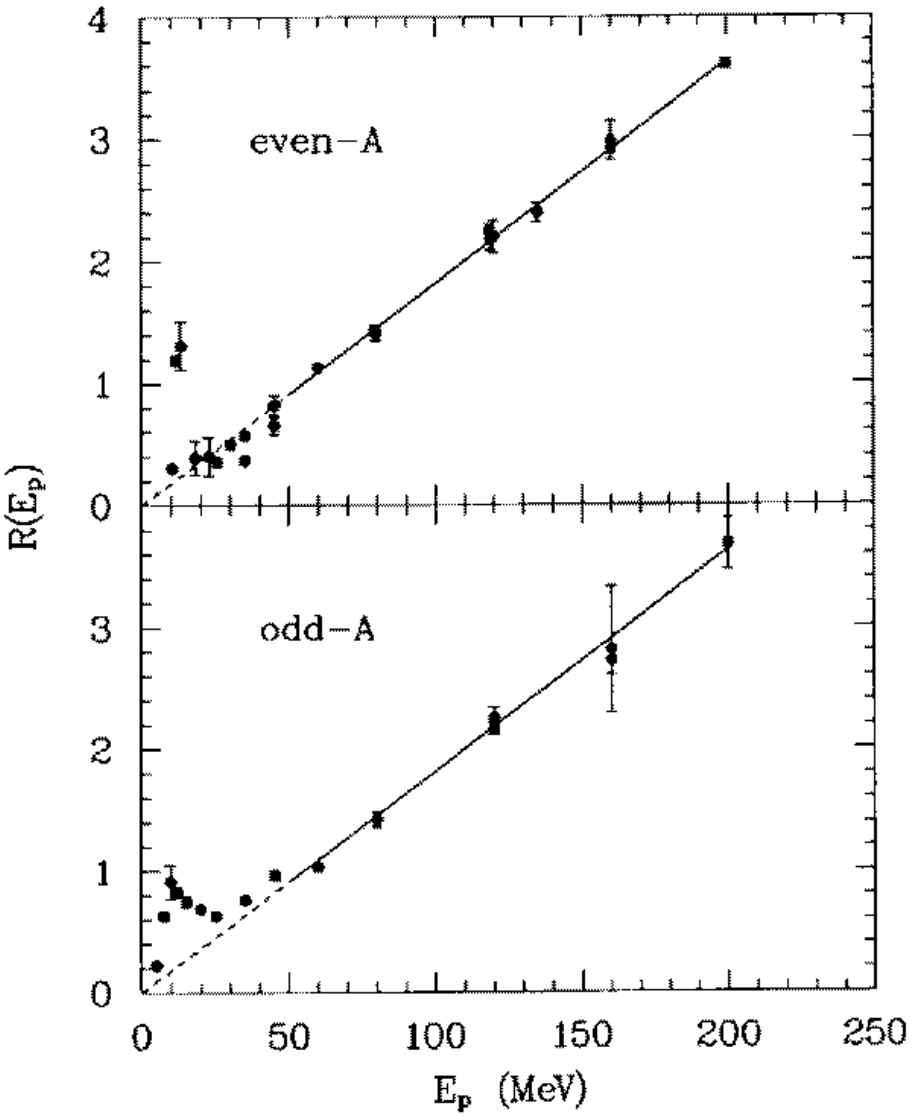

Figure 2.6: [TaG87] The quantity $R(E_p)$ determined from many target nuclei. The data points have been segregated into even–A and odd–A cases.

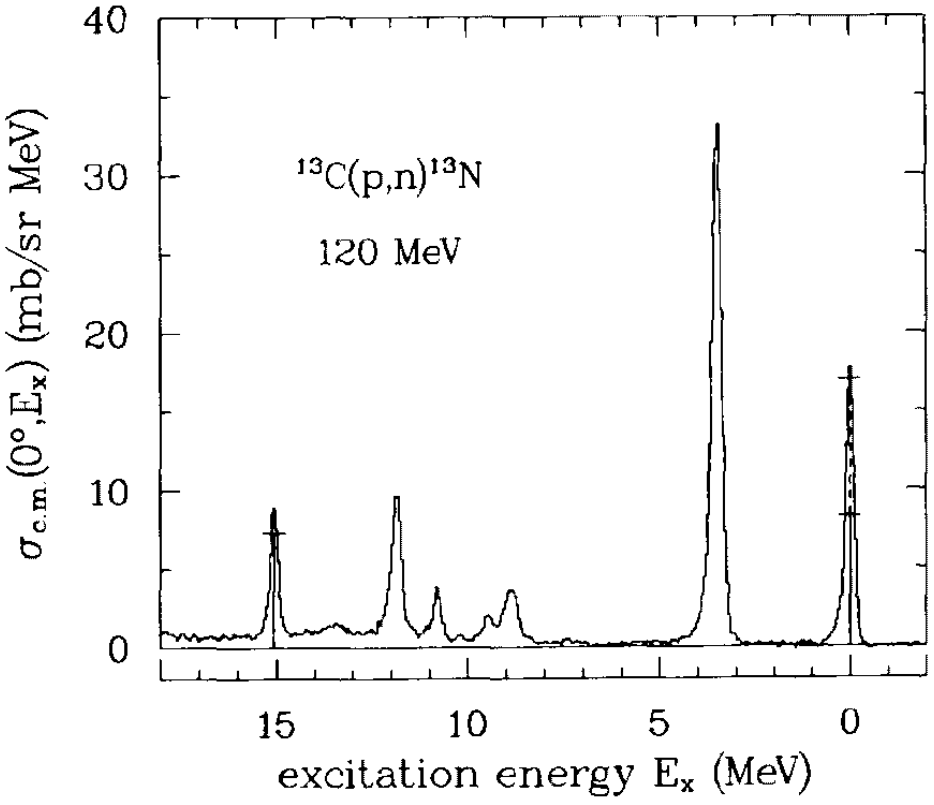

Figure 2.7: [TaG87] Cross section spectrum for ^{13}C(p,n) at 0° and 120 MeV. The vertical bars represent the GT transition strengths for analogous beta decays. The Fermi strength is indicated by the dashed vertical line.

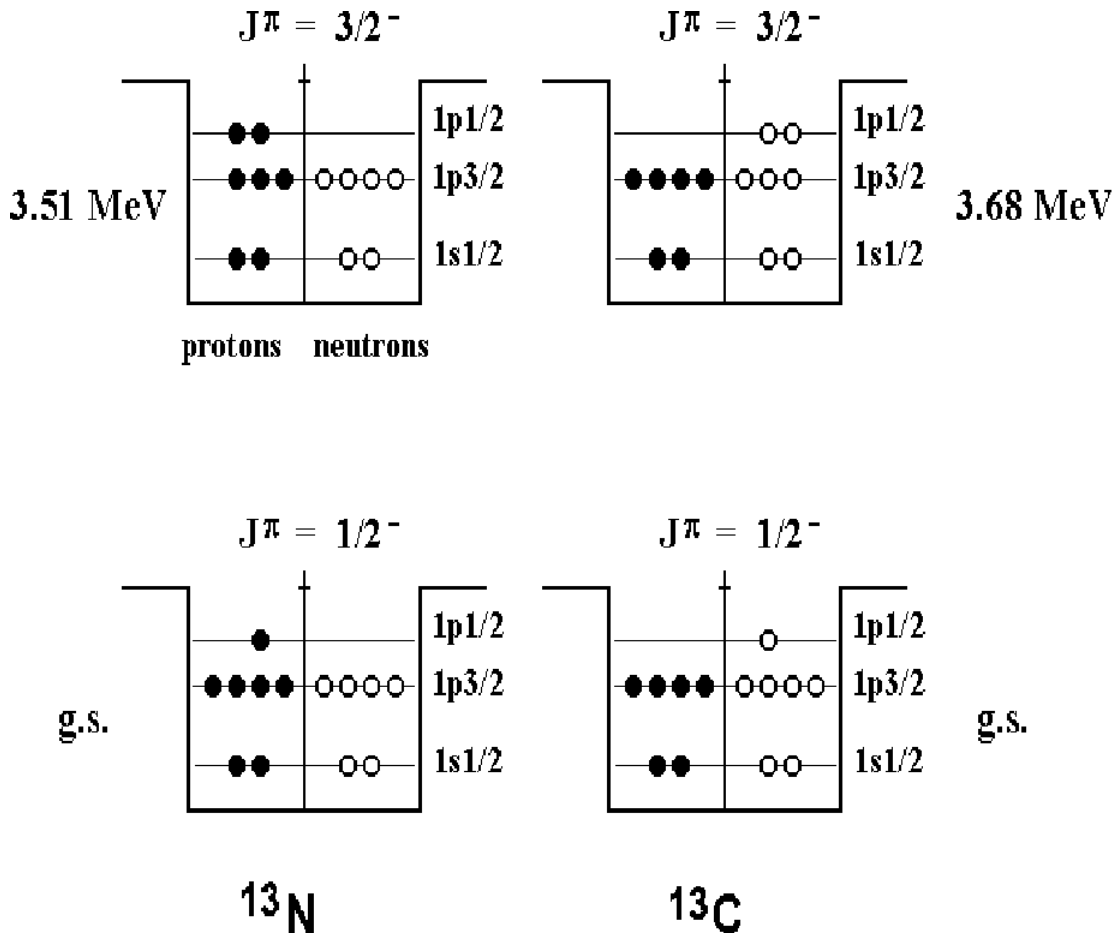

Figure 2.8: Schematic illustration of the nuclear configurations in ^{13}C and ^{13}N for the states under discussion. The ground state configurations are shown at the bottom. The states near 3.5 MeV are strongly excited in both ^{13}C(p,n) and ^{13}N(n,p) charge exchange (see Fig. 2.7).

are available from β-decay measurements. The Fermi and Gamow–Teller strengths for these states are indicated by the dashed and solid vertical lines, respectively. Fig. 2.8 illustrates the configurations involved in the transitions discussed here.

The argument centers on a comparison between the zero–degree cross sections measured for the lowest excitations in the reaction and B(GT) values obtained from shell–model calculations. The discussion is summarized as follows:

Using the measured zero–degree ^{13}C(p,n)^{13}N cross section at 160 MeV for the transition to the ^{13}N ground state, and normalizing the Fermi and GT contributions according to Eq. 2.10, Goodman et al. [GoB85] found a $\hat{\sigma}_{\rm GT}$ value of 12.7 mb/sr, which is large compared to e.g. the $\hat{\sigma}_{\rm GT} = 8.1$ mb/sr found for the ^{14}C(p,n)^{14}N reaction at the same proton energy. From the measured cross section and their $\hat{\sigma}_{\rm GT}$ value, the authors obtained B(GT) = 0.83 ± 0.03 for the $\frac{1}{2}^-$ to $\frac{3}{2}^-$ transition to the state at 3.68 MeV excitation energy in ^{13}N. The shell–model value for this state is B(GT)=2.38 [LeK80], which lead them to suggest that the B(GT) strength for this transition is quenched by a factor of 0.36, which is a larger effect by far than the usual quenching factor of approximately 0.60.

Further corroboration for the high $\hat{\sigma}_{\rm GT}$ value was originally found in the fact that the cross section for the transition to the $\frac{3}{2}^-$, T = $\frac{3}{2}$ state at 15.1 MeV, where the B(GT) is known from β–decay measurements, corresponds to $\hat{\sigma}_{\rm GT} = 13.8$ mb/sr. Later on, that measurement was shown to be in error due to an unexpectedly high amount of ^{12}C in the ^{13}C target, and subsequent zero–degree cross–section measurements of the ^{13}N(n,p)^{13}C and ^{13}C(p,n)^{13}N reaction at 200 MeV yielded values of $\hat{\sigma}_{\rm GT}^{\rm (n,p)} = 7.24 \pm 0.33$ mb/sr and $\hat{\sigma}_{\rm GT}^{\rm (p,n)} = 9.81 \pm 0.8$ mb/sr [MiA91]. It should be noted, however, that the erroneous value had no direct bearing on the $\frac{1}{2}^-$ to $\frac{3}{2}^-$ B(GT) measurement of Ref. [GoB85].

Watson et al. [WaP85] contended that the $\hat{\sigma}_{\mathrm{GT}}$ value used in Ref. [GoB85] was inflated by an unusually high GT cross section in the ^{13}C(p,n)^{13}N ground–state peak. They argued that this is due to renormalization of the Gamow-Teller operator in the nuclear medium, which has a tensor correction that is known to assume a maximum value for $\frac{1}{2}^-$ to $\frac{1}{2}^-$ transitions and causes an increase in the observed (p,n) cross sections [Wat94]. Their recalibration yielded B(GT) = 1.38 for the $\frac{1}{2}^-$ to $\frac{3}{2}^-$ transition, which represents a much more ordinary quenching of 0.58. The corresponding unit cross section is $\hat{\sigma}_{\mathrm{GT}} = 8.4\,\mathrm{mb/sr}$, quite comparable to other measurements at this energy.

However, there are arguments to support the results of Goodman et al. as well: The assignment of the Fermi and GT portions of the ground state cross section was repeated at a later date using polarization measurements [Rap95] and confirmed the earlier result.

In the present work, the value $\mathrm{B(GT)} = 0.83 \pm 0.03$ is used, since it represents the conventional approach and has not conclusively been shown to be in error. It is also the most recently available value in the literature [RaW87].

2.4 Heavy Ions as GT Probes

In recent years, heavy–ion charge exchange (HICEX) reactions have begun to attract interest as probes for GT strength, and experiments have been carried out to investigate the feasibility of the method [WiA86, WiA87, IcI94, Aus94].

The experimental methods available for measurements of GT strength in radioactive nuclei are limited. One obvious choice is to employ the (p,n) reaction in inverse kinematics, using radioactive beams on a hydrogen target. If good energy resolution is to be obtained, however, these experiments will be difficult, since they involve the

detection of rather low energy neutrons, and experiments in the β^+ direction are not possible, as there are no neutron targets.

HICEX offers several advantages over nucleon–induced charge–exchange reactions. Since it only involves charged particles, the energy resolution can in principle be very good. HICEX further offers favorable kinematics, the capability to sample both the β^+ and the β^- direction, and the additional advantage of quantum selectivity for certain projectile–ejectile choices. In the (^{6}Li,^{6}He) reaction, for example, final states can be chosen which limit the transitions to $\Delta S = 1, \Delta T = 1$ [WiA87].

The problems concerning the suitability of the HICEX reaction for spin–isospin spectroscopy are twofold: Firstly, the importance of contributions from sequential stripping and pickup of nucleons, such as [(^{6}Li,^{7}Li)(^{7}Li,^{6}He)], has to be investigated. Such studies — both experimental and theoretical — have been carried out for the (^{6}Li,^{6}He) [WiA87] and the (^{12}C,^{12}N) [WiA86, AnW91, LeW89] reaction at varying energies. The results of these studies indicate that for the (^{6}Li,^{6}He) reaction, the one–step process dominates above approximately E/A = 25 MeV, while two–step processes are important in the (^{12}C,^{12}N) reaction up to E/A = 50 MeV. Extrapolations from the detailed study by Lenske et al. [LeW89] lead to an estimated 30% two–step contamination in the forward cross section of the the (^{12}C,^{12}N) reaction near E/A = 60 MeV. The proportions might be expected to be similar for the ^{13}C(^{13}N,^{13}C)^{13}N reaction, since the GT strengths involved in both systems are comparable in magnitude.

The second, more involved question regards the effects of the finite size and structure of the projectile and has several facets. One issue is that the internal structure of the projectile allows additional amplitudes, not proportional to GT strength, to contribute to the cross sections. In contrast to (p,n) charge exchange, orbital angular

momentum as well as spin angular momentum can be transferred in the reaction, and different values of projectile and target orbital angular momentum can couple together to give the same angular–momentum transfer. For example, in the 0^+ to 1^+ transition of the (^{12}C,^{12}C) reaction, the L = 0 cross sections contains "cross terms", where $L_p = 0$ couples with $L_t = 2$ and vice versa [AnW91]. However, computations performed to investigate these amplitudes have found the contributions to be small [AnW91].

In this context, the (^{3}He,t) reaction deserves special mention, as all nucleons in the A=3 system are in the 1S state (L = 0), and no orbital angular momentum can be transferred to the projectile. This reaction is a valuable tool in its own right, combining the advantage of a charged ejectile with the relative simplicity of the (p,n) reaction, but also serves to bridge the gap between nucleon–induced and heavy–ion charge exchange [JäB94, AkD94].

A further complication, also connected with the size of the participants, concerns the strong absorption in heavy–ion reactions, which ensures that only the surface regions of the projectile and target transition densities are sampled in the reaction. This limitation to a narrow spatial region implies — by the uncertainty principle — that the reaction is sensitive to a large range of the momentum transfer q in the transition density. This should make the measured cross sections an unreliable measure of GT strength, which is equal to the corresponding transition density at $q \approx 0$. The issue has been studied in a theoretical experiment for the ^{26}Mg(^{12}C,^{12}N)^{26}Al reaction [AnW91], where the same wave functions were used to determine the B(GT) and cross section values, and a close proportionality between GT strength and cross section was found. This surprising behaviour was investigated by Osterfeld et al. [OsA92] using an eikonal model calculation. It was found that while the cross section did indeed involve an integral over all momentum transfers in the transition

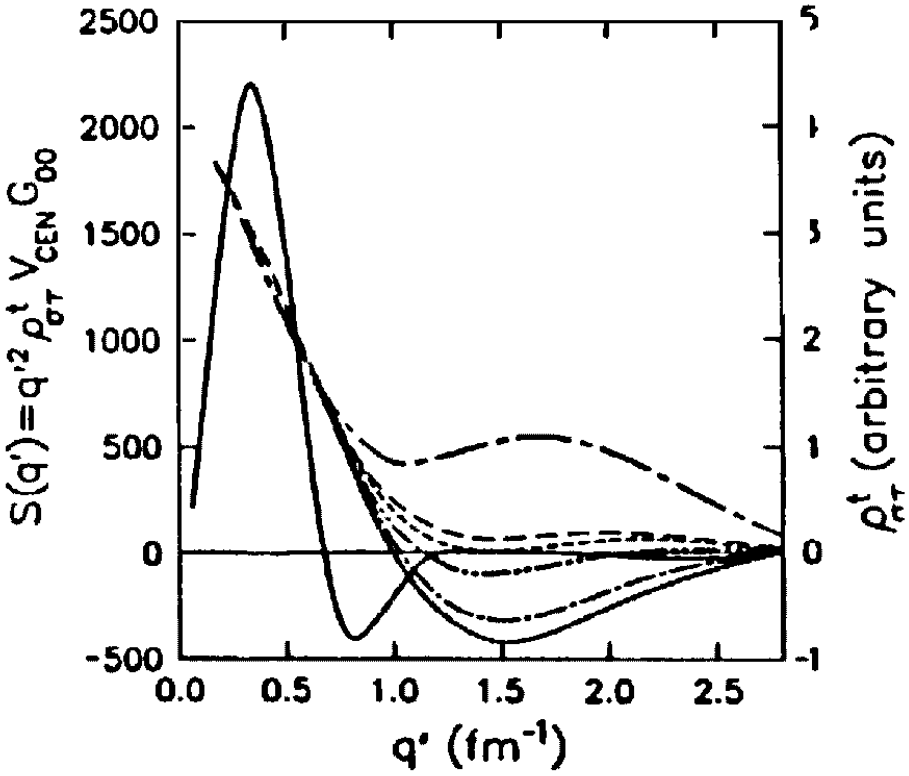

Figure 2.9: [Aus94] Comparison of the sensitivity function S(q) (solid line) and the transition densities for transitions to the lowest six 1^+ states of ^{26}Al in the ^{26}Mg(^{12}C,^{12}N)^{26}Al reaction at E/A = 70 MeV (dashed lines).

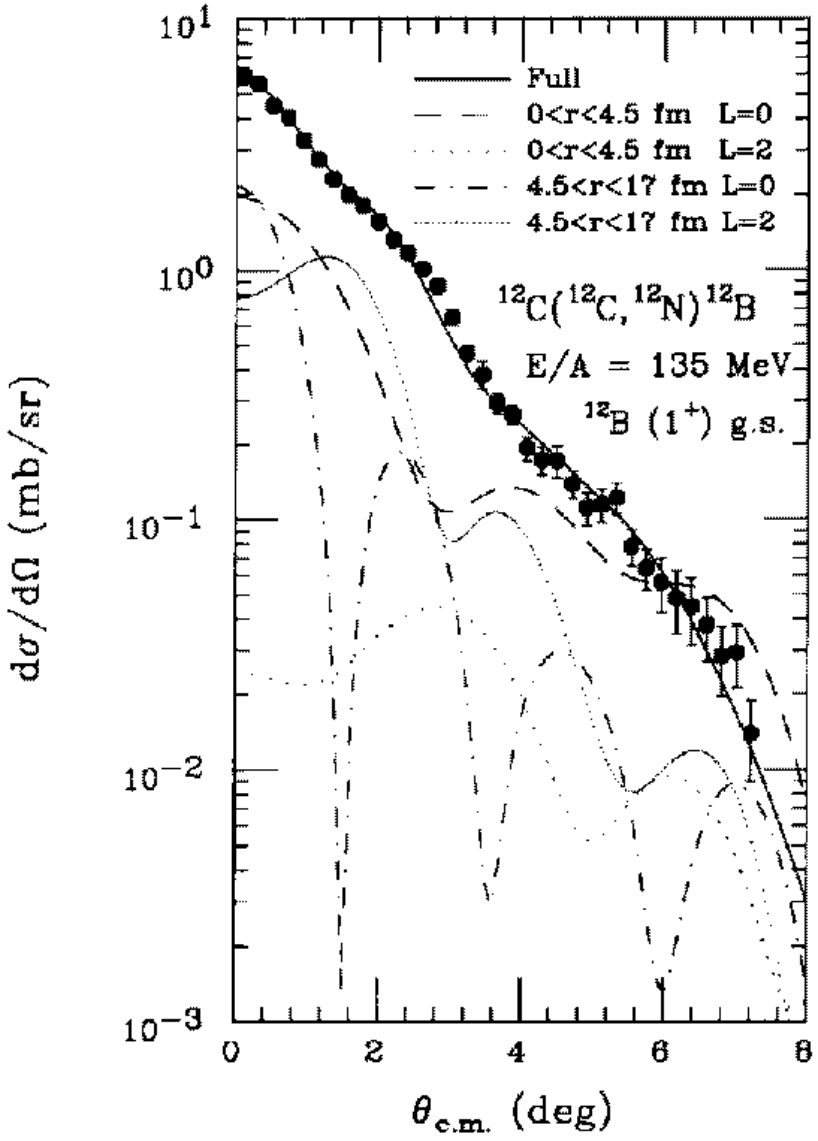

Figure 2.10: [IcI94] Cross section measurement near zero degrees for the ^{12}C(^{12}C,^{12}N)^{12}B reaction at E/A = 135 MeV. The lines show results of a DWBA calculation, described in the text.

density, these were weighed by a sensitivity function which limited contributions to a small range of q. This is illustrated in Fig. 2.9, which shows six different transitions densities, all normalized to the same peak value, together with the sensitivity function, peaked near q = 0.35 fm^{-1}. The observed specific proportionality is due to the fact that the shapes of the transition densities is nearly identical in the region selected by the sensitivity function. This illustrates an important advantage of mirror symmetry: Due to the structural similarity of the nuclei involved, only one set of transition densities enters the equations.

The strong absorption in heavy–ion reactions also influences the cross section directly by shielding large parts of the nuclear volumes from each other. This effect as well as the influence of the Q value on the reaction cross section are illustrated in the following example: Anantaraman et al. [AnW91] studied the ^{12}C(^{12}C,^{12}N)^{12}B reaction at E/A = 70 MeV as part of an effort to measure GT strengths in ^{56}Mn. A forward cross section of 1.4 mb/sr was measured for the 0^+ to 1^+ transition to the ground state in ^{12}B. By a careful analysis using the distorted–wave approximation, the L = 0 portion of the cross section was determined as $\sigma(\mathrm{L}=0,\,\theta=0) = 0.70$ mb/sr, with approximately a 10% error in overall normalization. Because of the large Q value of the reaction ($\mathrm{Q_{gs}} = -30.71$ MeV), the extrapolation to zero momentum transfer requires a large correction factor: $\mathrm{F}(\mathrm{q},\omega) = 6.81$, which makes the L = 0 portion cross section at zero degrees and zero momentum transfer

$$\sigma(\mathrm{L}=0,\theta=0,\mathrm{Q}=0) = 4.78\,\mathrm{mb/sr}. \tag{2.13}$$

When the same reaction was studied at E/A = 135 MeV by Ichihara et al. [IcI94] and a similar analysis performed, the measured forward cross section was $\sigma = 5.9$ mb/sr ($\pm 20\%$), with an L = 0 contribution of $\sigma(\mathrm{L}=0,\,\theta=0) = 4.5$ mb/sr. The extrapola-

tion to Q=0, yielded

$$\sigma(\mathrm{L}=0,\,\theta=0,\,\mathrm{Q}=0) = 14.8\,\mathrm{mb/sr}, \tag{2.14}$$

much higher than the 70 MeV result. In an effort to understand this discrepancy, a distorted–wave Born approximation (DWBA) calculation was carried out, in which the nuclear form factor was divided into an inner part ($0 < \mathrm{r} < 4.5\,\mathrm{fm}$) and an outer part ($4.5 < \mathrm{r} < 17\,\mathrm{fm}$), and the contributions of the inner and outer regions were studied separately. The result of this study is shown in Fig. 2.10. It is apparent that the contribution of the inner region of the form factor is nearly as large as that of the outer region near zero degrees. This behaviour is due to the increased nuclear transparency at higher energies. While both contributions are approximately 2.0 mb/sr, their coherent sum gives an L = 0 cross section of 4.8 mb/sr, indicating constructive interference. The L = 0 contribution from the outer part of the form factor only is 6.2 mb/sr, which is compatible with the 70 MeV measurement, where contributions from the inner region of the form factor are expected to be negligible.

While a consistent, microscopic understanding of the HICEX mechanism is still lacking, the studies cited above indicate that the reaction has the potential to become an important tool for GT strength measurements. One obvious disadvantage is the requirement to calibrate each reaction individually, as the overall proportionality factor appears to be even more variable than for the (p,n) reaction. However, HICEX is at present the most promising method for measuring the GT strength function in radioactive nuclei for all but the lightest isotopes. Especially in the astrophysically important region near the Fe peak, charge–exchange experiments with radioactive beams and nuclear targets will likely be the method of choice.

2.5 Other Charge–Exchange Probes

There are other experimental techniques, such as pion scattering or experiments with electromagnetic probes, that are relevant to the measurement of weak–interaction strength, but which are not discussed in the present work. For more information on these, the reader is referred to the review by Rapaport and Sugarbaker [RaS95].

Chapter 3

The Experiments

The mirror charge–exchange experiments were performed with the A1200 fragment separator operated in a dispersion–matched mode using an ^{14}N primary beam. The secondary ^{13}N beam was produced in a beryllium target located at the A1200 target position and was focused onto a ^{13}C reaction target, manufactured from ^{13}C–labelled polyethylene powder (see Appendix A). Detailed experimental parameters are given in table 3.1. The final ^{13}C reaction products were registered in a detector setup at the focal plane, which consisted of two position monitors, a position–sensitive silicon detector (PSD), and a thick plastic scintillator, providing measurements of two-dimensional position and angle, energy loss, total energy, and time–of–flight with respect to the cyclotron RF. Fig. 3.4 shows the setup schematically. The main challenges in performing the charge–exchange experiments were:

- Achieving good energy resolution despite the energy spread of the secondary beam
- Minimizing background while obtaining a sufficiently high secondary–beam rate
- Obtaining reliable cross–section measurements
- Measuring the angular distribution by ray tracing

Table 3.1: Experimental parameters for the Charge–Exchange experiments

NSCL Experiment Number	92065	93043
Primary Beam	^{14}N, E/A=70 MeV	^{14}N, E/A=120 MeV
Intensity (approx.)	50 pnA; 3×10^{11}s^{-1}	15 pnA; 1×10^{11}s^{-1}
Production Target	^{9}Be, 570 mg/cm^2	^{9}Be, 1100 mg/cm^2
^{13}N Energy	E/A=57 MeV	E/A=105 MeV
Intensity (approx.)	5×10^{6}s^{-1}	6×10^{5}s^{-1}
Reaction Target	$^{13}CH_2$, 9.0 mg/cm^2	$^{13}CH_2$, 18.0 mg/cm^2
Energy Spread (fwhm)	15 MeV	27 MeV
Second Stage Dispersion	3.6 $\frac{\text{cm}}{\%}$	4.1 $\frac{\text{cm}}{\%}$
^{13}N Resolution (fwhm)	1.0 MeV, E/ΔE=750	1.5 MeV, E/ΔE=900
^{13}C Resolution	2.0 MeV	2.4 MeV
$^{13}N^{6+}/^{13}N^{7+}$ Ratio	$(1.0\pm0.1)\times10^{-5}$	$(1.5\pm0.2)\times10^{-6}$

The following sections address these issues and may be used as a reference for future radioactive–beam experiments. The two experiments were sufficiently similar in design and execution that figures from both experiments are shown and discussed interchangeably.

3.1 Secondary–Beam Production

The optimum production target is thick enough to produce the desired secondary beam in sufficient intensity, but at the same time thin enough not to cause broadening of the ions' momentum distribution too far beyond the acceptance of the spectrometer. While moderate gains in usable secondary–beam intensity are possible with very thick targets, the introduction of a wider variety of isotopes into the acceptance window adds difficulties that must be taken into account. Target thicknesses for the mirror charge–exchange experiments are listed in Table 3.1.

With the production targets in place, the first step in the experiments was to determine the magnetic rigidity that would produce the maximum number of ^{13}N nu-

clei. This was achieved by varying the magnetic rigidity with the entire spectrometer set to the same Bρ and observing the ^{13}N rate.

The top of Fig. 3.1 shows an energy–loss/time–of–flight spectrum recorded at the optimum Bρ setting, with several isotopes identified. This is a very typical particle identification spectrum, with the N=Z nuclei all arriving at the focal plane with nearly identical time of flight. Note the absence of unstable ^{8}Be, which provides a convenient clue to particle identification. While the presence of nuclei with mass number smaller than 14 is attributed to nuclear fragmentation, ^{14}N itself should not be detected, as the magnetic rigidity of the primary beam after the target does not fall within the acceptance of the spectrometer. Due to the high number of incident particles, however, even a small fraction of the primary beam scattering off an aperture and producing secondary reaction products could produce significant amounts of contamination. Scattered primary beam is indeed evident in nearly all fragmentation experiments over a wide range of magnetic rigidities that are smaller than the Bρ of the beam. In order to minimize the amount of ^{14}N reaching the reaction target, the primary beam was put through the production target at an angle of about 1° horizontally. This was achieved by steering the beam towards the positive x coordinate with a horizontal dipole magnet, located approximately 2.7 m before the production target, and then steering it back on the center of the target with the quadrupole elements of the beam line, which act as bending magnets for beams that are off–center. The E/A = 57 MeV experiment was performed using the "Low–Acceptance" target position, and the primary–beam particles not reacting in the target were dumped on water–cooled slits located approximately 1800 mm downstream of the target position. In the 105 MeV experiment, however, the production target was moved upstream to the so–called "Mid–Acceptance" position in order to take advantage of a newly installed quadrupole doublet, located immediately upstream of the Mid–Acceptance

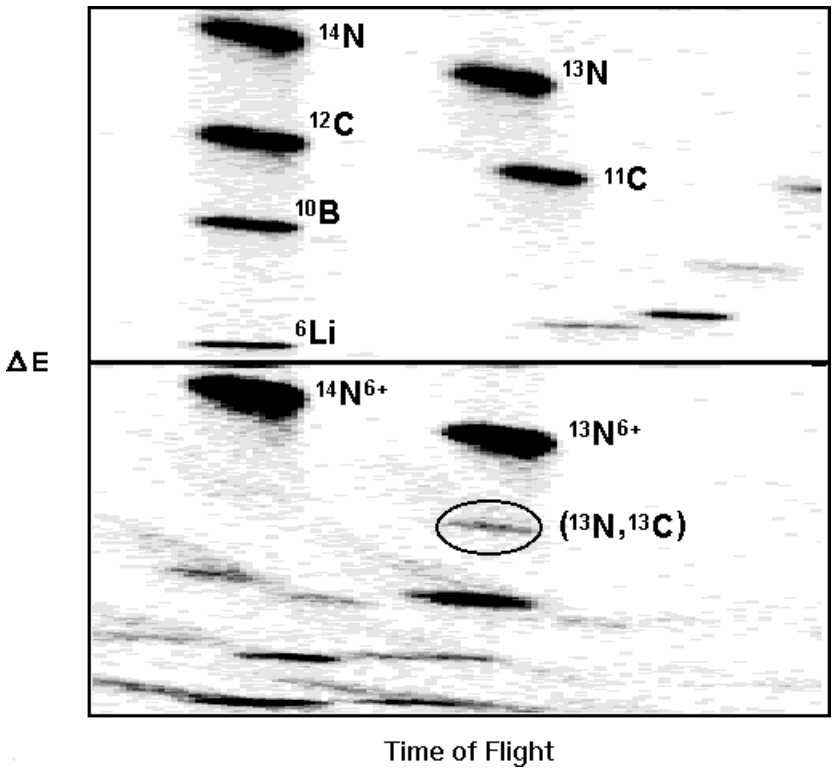

Figure 3.1: ΔE-TOF particle–identification spectra obtained with the entire A1200 set to the magnetic rigidity of the ^{13}N fragments (top) and with the magnetic rigidity of the second dipole stage scaled by a factor of 7/6 to collect the ^{13}C reaction products (bottom). The bottom spectrum was recorded with a primary–beam intensityh five orders of magnitude higher than for the top spectrum. The large amount of background is clearly visible. The desired ^{13}C particles are marked by the oval.

position. A horizontal beam spot size of approximately 0.5 mm across was achieved, compared with about 1 mm in the earlier experiment. Instead of using the slit drives, which cannot be adjusted to less than 3 mm full opening, water–cooled aperture plates were used, located only 95 mm downstream of the Mid position. Two different round apertures were used during the experiment, 1/32"and1/16" in opening diameter. The short distance from beam spot to aperture made the secondary–beam properties very sensitive to slight changes in the position of the primary beam.

The importance of angling the primary beam to prevent it from entering the spectrometer should be emphasized; an early test run begun without this technique [StB91] suffered from background so intense that it rendered the ^{13}C group invisible.

With the magnetic rigidity of the second dipole stage increased by a factor of 7/6 to accept the (^{13}N,^{13}C) reaction products, the spectrum at the bottom of Fig 3.1 was obtained. The primary–beam intensity was approximately five orders of magnitudes higher than for the previous spectrum. ^{14}N and ^{13}N appear in the same position as before, but in their 6+ charge state. The ^{13}C reaction products, which have very nearly the same velocity as the ^{13}N secondary beam, appear at the same time–of–flight, but at lower energy loss, due to their lower nuclear charge. They are visible inside the oval. Other particle groups come in two different varieties: Those that have the same general shape and size as the original isotopic clusters and are due to nuclear reactions of contaminants, and those that are smeared out diagonally over relatively large areas. The latter are attributed to particles scattering off beam line walls or apertures and their secondary reaction products. Note that one such group is intruding into the ^{13}C cluster from above. In chapter 4, the amount of background particles in the (^{13}N,^{13}C) spectra will be shown to be correlated with the amount of ^{14}N present.

3.2 Cross–Section Measurements

Two quantities have to be known in order to determine the reaction cross sections: the number of ^{13}C atoms per unit area in the reaction target and the number of incident ^{13}N ions. The number of target atoms was obtained from the measured weight and area of the target, together with the chemical composition of the target material. Fig. 3.2 shows the energy–calibrated position spectra collected simultaneously for the $^{13}C(^{13}N,^{13}C)^{13}N$ reaction products and the $^{13}N^{6+}$ secondary beam at E/A = 105 MeV. The incident ^{13}N intensity was determined by monitoring the intensity of the $^{13}N^{6+}$ peak and dividing it by the 6+/7+ charge state ratio, ϵ. In the 57 MeV experiments, ϵ was determined by adjusting the magnetic rigidity of the second dipole stage to select $^{13}N^{7+}$ and $^{13}N^{6+}$, respectively, counting the number of particles arriving at the focal plane, and monitoring the beam current using four "beam monitors". These are small silicon detectors mounted around the production target that measure scattered beam particles and provide an excellent relative measure of beam current.

Since these detectors were unavailable in the 105 MeV experiment, the charge–state ratio was determined by a direct measurement. Two parallel–plate avalanche counters (PPACs) located at the dispersive image plane were used to monitor the incoming $^{13}N^{7+}$ beam, and the $^{13}N^{6+}$ leaving the reaction target were collected at the focal plane. Since the count rate observed in the PPACs ceases to be proportional to the number of incoming particles at rates above approximately 5000 particles per second, the PPAC response was calibrated by sending the $^{14}N^{7+}$ primary beam through the A1200 at varying intensities and counting ions in the PPACs as well as in the PSD – which is assumed to have 100% efficiency.

With either method, the accuracy obtained for ϵ is estimated to be no worse than 10%. The results are listed in Table 3.1.

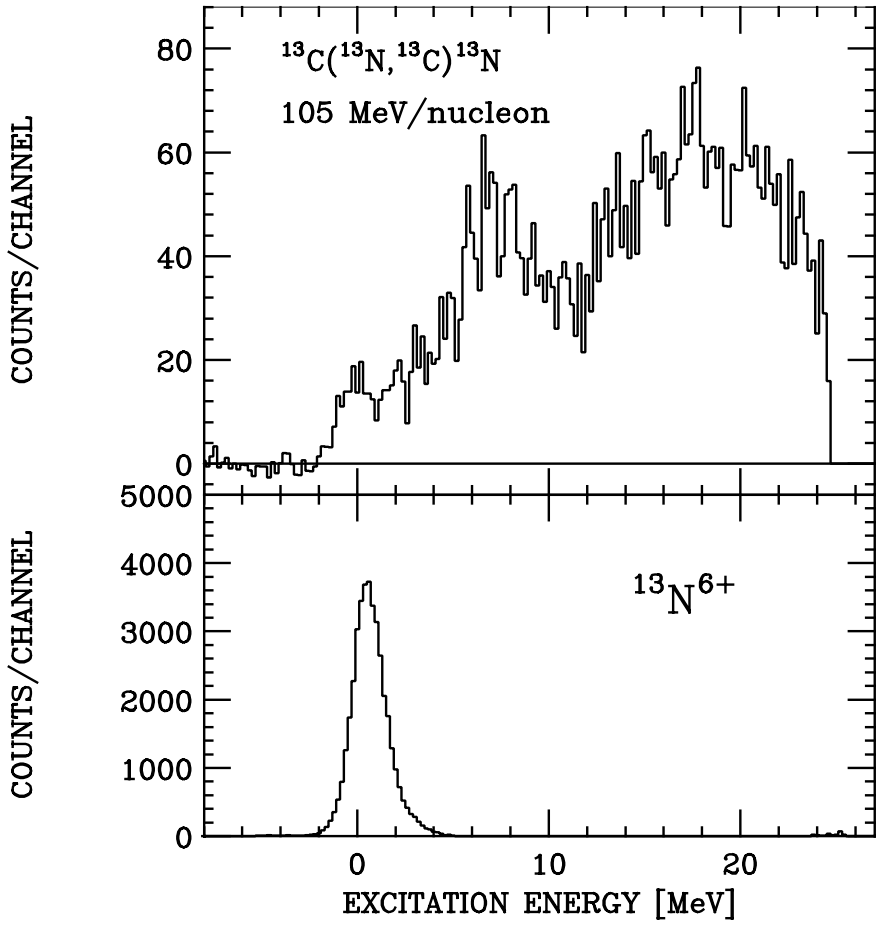

Figure 3.2: Energy–calibrated position spectra for the (^{13}N ,^{13}C) reaction products (top) and the $^{13}N^{6+}$ charge state (bottom) at E/A = 105 MeV. The $^{13}N^{6+}$ peak provides a convenient method of monitoring the secondary–beam intensity and also supplies the absolute calibration of the energy scale.

3.3 Ion Optics

The present section is a quick review of the basics of charged–particle optics. For a comprehensive introduction, see e.g. [Wol87].

It is convential in ion optics to define the position of a charged particle as a vector in a six–dimensional phase space, with the coordinates given with respect to a reference particle, thought to move along the optical axis of the device with the desired momentum. The coordinates used are x, the horizontal distance of the particle from the optical axis; θ, the angle between the particle trajectory, projected onto the horizontal plane, and the optical axis; y and ϕ, the vertical position and angle; l, defining the distance between the ion and the reference particle along the optical axis; and δ, the deviation of the ion's momentum from that of the reference particle. Units used conventionally for the six coordinates are cm and mrad for the position and angle coordinates, and % in Δp/p for momentum. The coordinate z, with units of m, describes the reference position along the optical axis. The l coordinate is not of interest in the present case, but is carried along for reasons of convention.

The optics of a beam transport system are expressed as a matrix equation in the form of a Taylor expansion. If the final (image) coordinate $\mathrm{x_f}$, for example, is a function of the initial (object) coordinates, $\mathrm{x_f} = \mathrm{f}(\mathrm{x_i}, \theta_\mathrm{i}, \mathrm{y_i}, \phi_\mathrm{i}, \delta)$, the Taylor series reads:

$$\mathrm{x_f} = \frac{\partial \mathrm{f}}{\partial \mathrm{x}}\,\mathrm{x_i} + \frac{\partial \mathrm{f}}{\partial \theta}\,\theta_\mathrm{i} + ... + \frac{1}{2!}\frac{\partial^2 \mathrm{f}}{\partial^2 \mathrm{x}}\,\mathrm{x_i^2} + \frac{1}{2!}\frac{\partial^2 \mathrm{f}}{\partial \mathrm{x}\partial\theta}\,\mathrm{x_i}\,\theta_\mathrm{i} + ... \qquad (3.1)$$

It is conventional to write e.g. the partial derivative $\frac{\partial^2 \mathrm{f}}{\partial\theta\partial\phi}$ as $(\mathrm{x}|\theta\phi)$. The first–order terms usually dominate the overall optical properties, and the first–order equation is given by an equation of the form $\vec{\mathrm{x}}_\mathrm{f} = \mathbf{A}\vec{\mathrm{x}}_\mathrm{i}$. $\mathbf{A}$ is called the transfer matrix. The full equation reads:

$$\begin{pmatrix} \mathrm{x} \\ \theta \\ \mathrm{y} \\ \phi \\ \mathrm{l} \\ \delta \end{pmatrix}_{\mathrm{f}} = \begin{pmatrix} (\mathrm{x}|\mathrm{x}) & (\mathrm{x}|\theta) & (\mathrm{x}|\mathrm{y}) & (\mathrm{x}|\phi) & (\mathrm{x}|\mathrm{l}) & (\mathrm{x}|\delta) \\ (\theta|\mathrm{x}) & (\theta|\theta) & (\theta|\mathrm{y}) & (\theta|\phi) & (\theta|\mathrm{l}) & (\theta|\delta) \\ (\mathrm{y}|\mathrm{x}) & (\mathrm{y}|\theta) & (\mathrm{y}|\mathrm{y}) & (\mathrm{y}|\phi) & (\mathrm{y}|\mathrm{l}) & (\mathrm{y}|\delta) \\ (\phi|\mathrm{x}) & (\phi|\theta) & (\phi|\mathrm{y}) & (\phi|\phi) & (\phi|\mathrm{l}) & (\phi|\delta) \\ (\mathrm{l}|\mathrm{x}) & (\mathrm{l}|\theta) & (\mathrm{l}|\mathrm{y}) & (\mathrm{l}|\phi) & (\mathrm{l}|\mathrm{l}) & (\mathrm{l}|\delta) \\ (\delta|\mathrm{x}) & (\delta|\theta) & (\delta|\mathrm{y}) & (\delta|\phi) & (\delta|\mathrm{l}) & (\delta|\delta) \end{pmatrix} \begin{pmatrix} \mathrm{x} \\ \theta \\ \mathrm{y} \\ \phi \\ \mathrm{l} \\ \delta \end{pmatrix}_{\mathrm{i}} .$$

In most instances, dipole and quadrupole elements are adjusted to provide the desired first–order imaging characteristics, while sextupoles and other higher–order lenses are used to minimize second–order effects. Some aberrations are excluded ab initio by taking advantage of certain symmetries in the design of the beam transport system. For example, symmetry around the horizontal plane defined by $\mathrm{y} = 0$ ("mid-plane symmetry") requires that two rays with the same overall coordinates and the same magnitude but opposite signs in ϕ_{i} be transported to the same final coordinate $\mathrm{x_f}$. Generally, midplane symmetry results in the condition $(\mathrm{x}|\mathrm{y}^{\mathrm{m}}\phi^{\mathrm{n}}) = 0$ if $\mathrm{m} + \mathrm{n}$ odd.

Also, many of the first–order terms are automatically equal to zero because of symmetry considerations; vertical and horizontal coordinates, for instance, are decoupled from each other, and in any system where the bend plane is horizontal, only the x coordinate can have first-order momentum dependence. The first–order matrix to be considered here has the following form:

$$\begin{pmatrix} (\mathrm{x}|\mathrm{x}) & (\mathrm{x}|\theta) & 0 & 0 & 0 & (\mathrm{x}|\delta) \\ (\theta|\mathrm{x}) & (\theta|\theta) & 0 & 0 & 0 & 0 \\ 0 & 0 & (\mathrm{y}|\mathrm{y}) & (\mathrm{y}|\phi) & 0 & 0 \\ 0 & 0 & (\phi|\mathrm{y}) & (\phi|\phi) & 0 & 0 \\ 0 & 0 & 0 & 0 & 1 & 0 \\ 0 & 0 & 0 & 0 & 0 & 1 \end{pmatrix}$$

Conservation of phase space density imposes the additional condition that the determinants of the horizontal and vertical submatrices be 1.

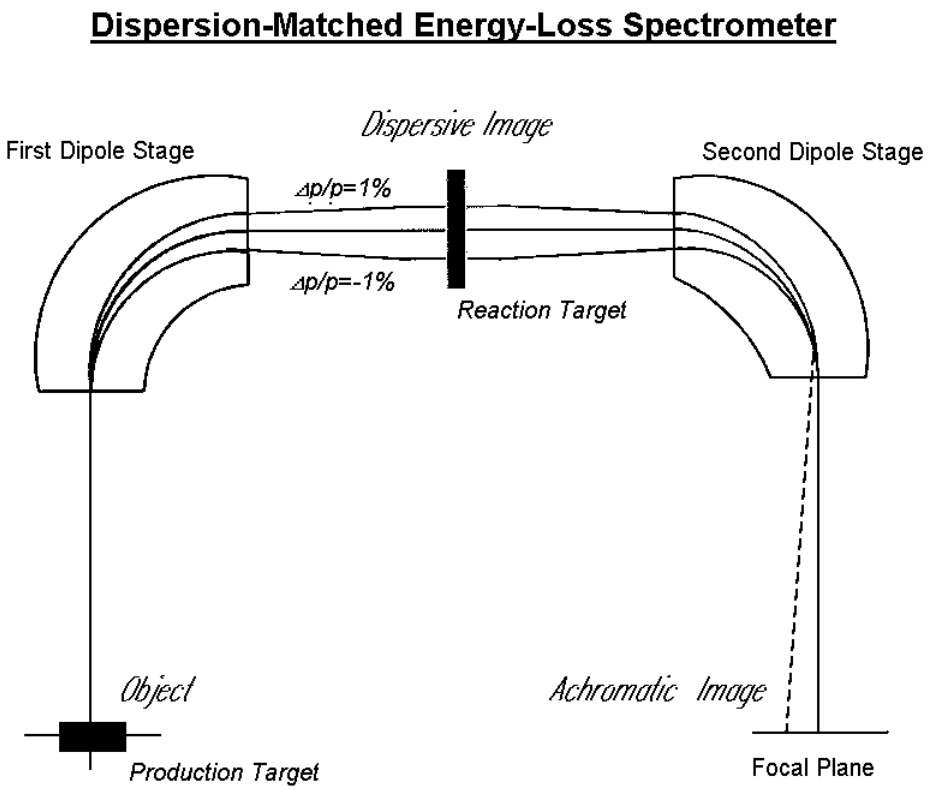

Figure 3.3: Principle of the energy–loss mode. The solid lines illustrate the principle of dispersion matching: Particles leaving the object (production target) with different magnetic rigidity are focused to a point at the final achromatic image (focal plane). If energy is lost in the reaction target, for instance due to excitation of a target nucleus, the particle will be displaced at the focal plane, as indicated by the dashed line. This displacement is independent of the original momentum.

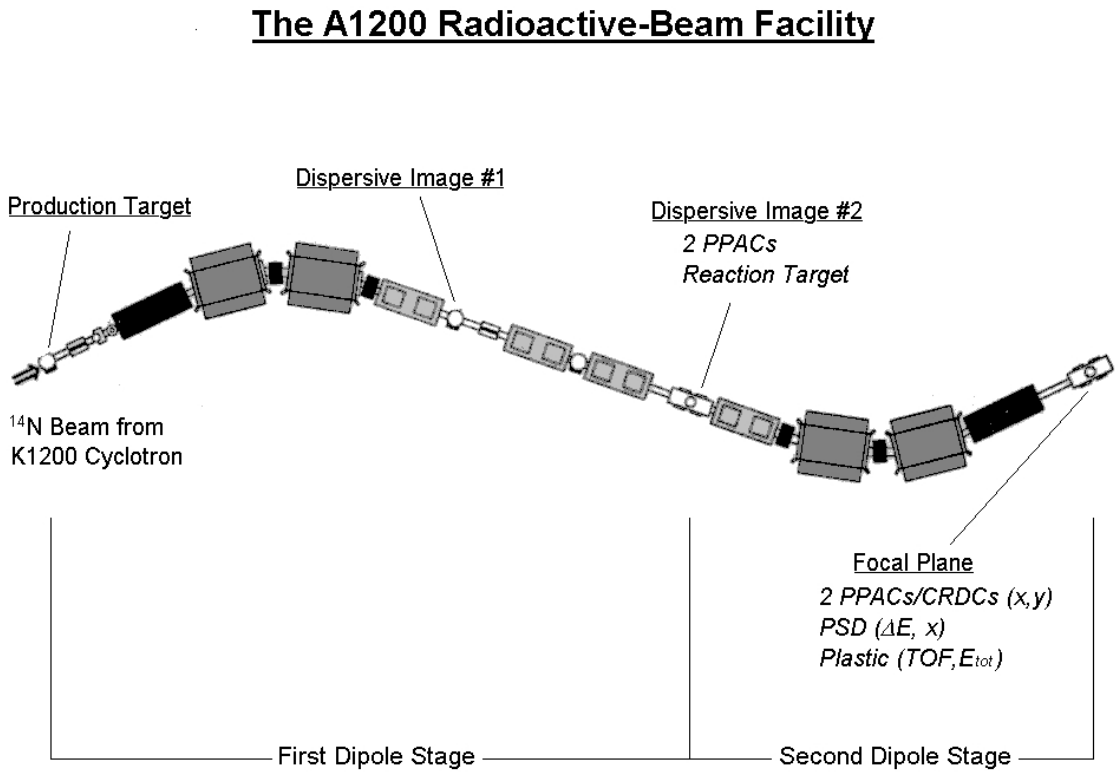

Figure 3.4: The A1200 Fragment Separator.

3.3.1 A1200 in Dispersion–Matched Mode

Radioactive beams produced by projectile fragmentation generally have large emittances. It is still possible, however, to perform high–resolution experiments with beams of poorly defined momentum by using a fragment separator in dispersion–matched mode, also known as energy–loss mode [ShM91].

The principle is illustrated in Fig. 3.3: The secondary beam particles leave the production target with a wide range of momenta and are focused by an initial dipole stage onto an image plane in the mid–section of the spectrometer. The beam spot at this dispersive image is large in the horizontal (bend) coordinate, and position is correlated with momentum, as indicated by the lines in the figure [$(\mathrm{x}|\delta) \neq 0$]. The second dipole stage is tuned to cancel the dispersive effect of the first, which leads to the condition $(\mathrm{x}|\delta) = 0$. Furthermore, the final angle θ_f must not depend on momentum, which would degrade the angular resolution: $(\theta|\delta) = 0$. If both conditions are met simultaneously, the system is said to be achromatic. In this situation, the only effect of the spectrometer – to first order – is to impose a cut in magnetic rigidity ($\mathrm{B}\rho$) on the beam, eliminating the primary beam and most of the unwanted reaction products. If a reaction target is placed at the dispersive image, and the magnetic rigidity of the second stage of the spectrometer is set to accomodate the reaction products, these will again be focused to a point at the final focal plane, provided the overall tune of the system is preserved. Energy lost in the reaction due to a nuclear excitation, however, will be missing from the ejectile's kinetic energy, causing it to be displaced at the focal plane, as indicated by the dashed line in Fig. 3.3. Excitation energy is determined from the focal–plane position spectrum after it has been calibrated (see Sec. 3.3.3).

More rigorously, the position $\mathrm{x_f}$ at the focal plane as a function of the coordinates

at the *reaction target* is (to first order)

$$x_f = (x|x)\, x_r + (x|\delta)\, (\delta_B + \delta_R), \tag{3.2}$$

where focusing $[(x|\theta) = 0]$ is assumed and δ_B and δ_R are the momentum coordinate of the beam and that induced by the reaction, respectively. The matrix elements describe the properties of the second dipole stage. Dispersion matching implies

$$(x|x)\, x_r + (x|\delta)\, \delta_B = 0, \tag{3.3}$$

so that the position x_f at the focal plane is independent of δ_B and a measure of δ_R only. Going back one step, the position x_r at the dispersive image in terms of the coordinates at the production target is given by

$$x_r = (x|x)^1\, x_i + (x|\delta)^1\, \delta_B, \tag{3.4}$$

where the superscript denotes matrix elements describing the first stage of the system. Assuming negligible initial beam–spot size, equation 3.3 becomes

$$\Big((x|x)(x|\delta)^1 + (x|\delta)\Big)\ \delta_B = 0. \tag{3.5}$$

This illustrates the fact that dispersion matching does not require equal and opposite dispersions $(x|\delta)$: Because the beam spot at the dispersive image is large, the magnification of the second dipole stage is important as well.

3.3.2 Optical Modes

Fig. 3.5 shows some characteristics of the so–called Medium–Acceptance Mode. Much like in geometrical optics, rays emerging from a point at the object (production target) come back to a point at the real image, as indicated by the beam envelope. This so-called 'point–to–point focusing' is employed in the x and y coordinates throughout the device and is illustrated in the figure for the horizontal direction: images occur

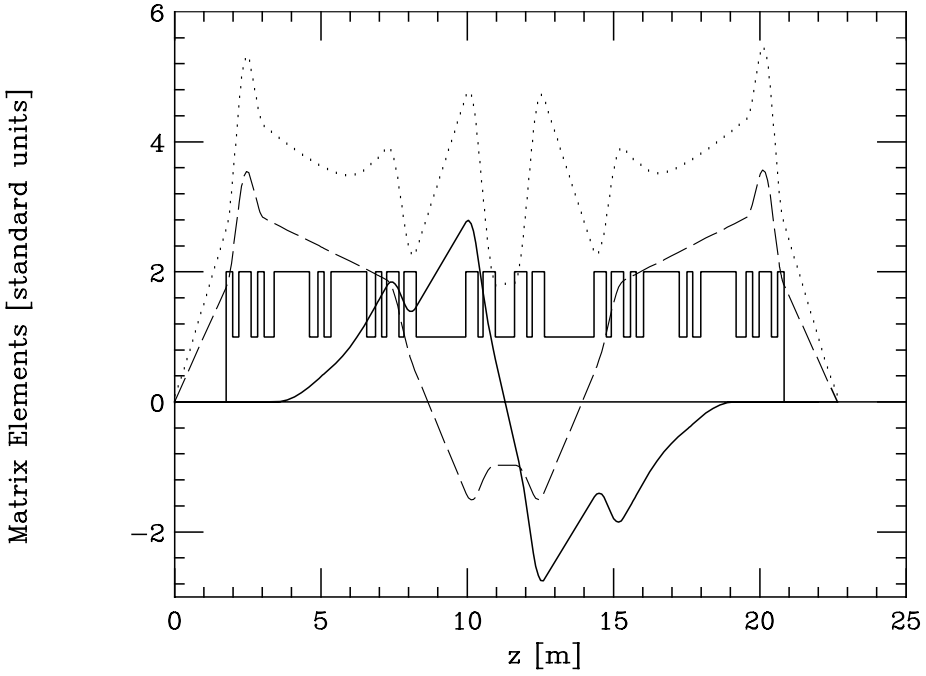

Figure 3.5: A1200 in Medium–Acceptance Mode. The figure shows the result of a TRANSPORT calculation. The horizontal beam envelope (dotted line) and the matrix elements $(x|\theta)$ (dashed line) and $(x|\delta)$ (solid line) are shown as a function of position along the optical axis. Units are cm, cm/mrad $\times 0.1$, and cm/%, respectively. The histogram indicates the location of the magnetic elements of the A1200, beginning with a quadrupole triplet, followed by a dipole segment, a sextupole, another dipole segment, and so forth. The zero crossings of $(x|\theta)$ indicate the target position ($z = 0$), the intermediate images Nos. 1 and 2, and the final image at the focal plane ($z = 22.65$ m). The size of the envelope is a function of angular size as well as momentum spead of the beam, and becomes small only at the focal plane, where $(x|\theta) = (x|\delta) = 0$.

wherever the $(x|\theta)$ matrix element is zero, since at these points, the first–order vector equation for x reduces to $x_f = (x|x)x_i$, with no angular dependence. The overall dispersion matching of the system is illustrated by the $(x|\delta)$ line, which goes to zero after the last dipole magnet.

The Medium–Acceptance mode is the optical mode used most often in the A1200 and provides straightforward raytracing as well as small focal–plane beam spots in both the x and y coordinates.

In the present experiments, however, a different mode was used, known as Reaction Mode. In this optical mode, the vertical angular acceptance in the second dipole stage of the spectrometer is much larger than in Medium–Acceptance Mode. This makes it ideal for secondary–beam experiments using a reaction target at the dispersive image No. 2, since the angular distribution of the final reaction products is usually much wider than that of the secondary beam, which is routinely limited in angle by apertures at the production target.

The tradeoff is that while the focusing in the horizontal coordinate is point–to–point throughout the device, it is "point–to–parallel" for the vertical coordinate in the second dipole stage. This means that trajectories emerging from a point at the reaction target with different angles are parallel to each other but have different y positions at the focal plane. Fig. 3.6 illustrates this. The $(x|x), (x|\theta), (y|y)$, and $(y|\phi)$ matrix elements are shown as a function of z for the area around the A1200 focal plane as predicted by a TRANSPORT calculation [BrR77]: The image in x [i.e. $(x|\theta) = 0$] coincides with the physical position of the focal–plane detectors as well as the point where vertical point–to–parallel focusing occurs [$(y|y) = 0$]. In reality, the x focus was adjusted to occur at the silicon PSD, but the $(y|y) = 0$ point was off by several cm. TRANSPORT calculations typically provide a good estimate of

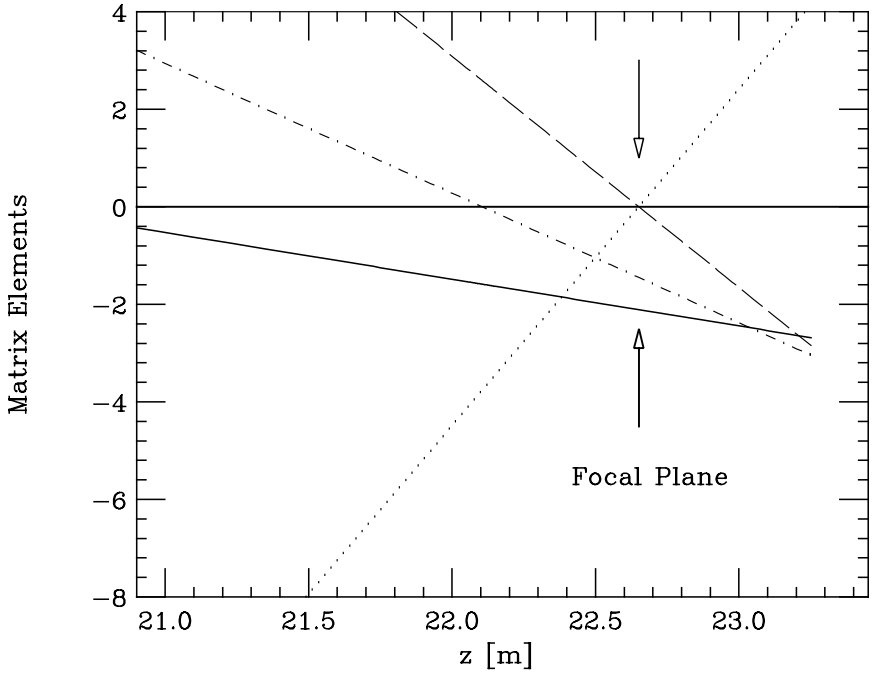

Figure 3.6: A1200 in Reaction Mode. The figure shows the matrix elements (x|x) (solid), (x|θ) $\times$ 0.01 (dashed), (y|y) (dot-dashed), and (y|ϕ) $\times$ 0.01 (dotted) as a function of position along the optical axis. The range is limited to the area around the focal plane and the standard units are used. The position of the position–sensitive silicon detector is indicated by the two arrows and coincides with the x focus as well as the (y|y) = 0 plane. Angles $\theta_{\rm i}$ and $\phi_{\rm i}$ at the reaction target are related to focal–plane coordinates through the first–order equations $\theta_{\rm f} = (\theta|\theta)\theta_{\rm i}$ and $y_{\rm f} = (y|\phi)\phi_{\rm i}$.

the overall optical properties, but individual conditions and matrix elements have to be determined experimentally. The agreement between calculated and measured matrix elements varies, but is often not too impressive. Some examples of measured (calculated) values for the second dipole stage are: $(\theta|\theta) = -0.65$ (-0.44), $(\mathrm{y}|\phi) = -0.022$ $(-0.013)\,\mathrm{cm/mrad}$, and $(\mathrm{x}|\delta) = 4.4$ $(4.5)\,\mathrm{cm/\%}$.

3.3.3 Dispersion and Energy Calibration

The energy scale was determined using the secondary ^{13}N beam with several settings for the magnetic rigidity of the second dipole stage. Fig. 3.7 shows the magnetic rigidity vs. beam spot position at the focal plane as obtained in the 105 MeV experiment. The line represents a linear least–squares fit to the data, which forms the basis for the energy calibration. Energy, momentum, and magnetic rigidity are linked to each other through the following equations:

$$\mathrm{B}\rho = \frac{\mathrm{p}}{\mathrm{q}}\,; \quad \mathrm{pc} = \sqrt{2\mathrm{mc^2E} + \mathrm{E^2}}; \quad \mathrm{E} = \mathrm{T} + \mathrm{mc^2},$$

where p, q, and m are the momentum, charge, and mass of the ion, and E and T are its total and kinetic energy, respectively. The dispersion $(\mathrm{x}|\delta)$ was found to be $3.6\,\frac{\mathrm{cm}}{\%}$ $(4.1\,\frac{\mathrm{cm}}{\%})$ in the 57 MeV (105 MeV) experiment and determined the slope of the energy calibraton. The E = 0 point was fixed by measuring the energy loss of the ^{13}N beam in the reaction target. From this value, the thickness of an equivalent ^{12}C target was obtained and the difference in energy loss for ^{13}N and ^{13}C was calculated. The zero of the energy scale was then determined for the ^{13}C(^{13}N,^{13}C)^{13}N reaction products, with the reaction taking place at half the target thickness. The broadening of the ^{13}C peaks due to differential energy loss is taken into account during the data analysis.

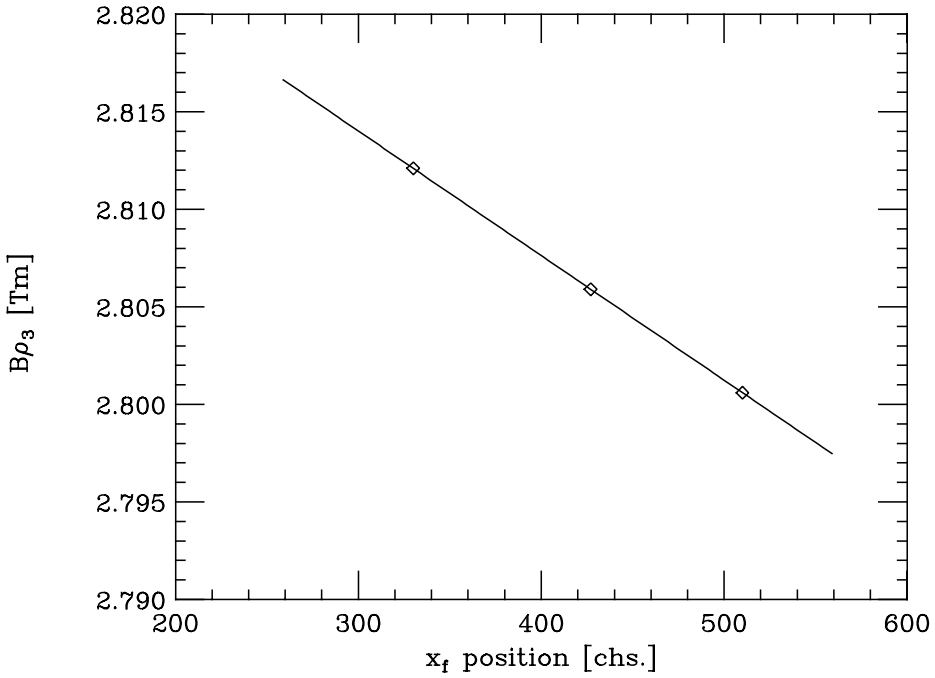

Figure 3.7: Bρ_3 vs. x_f calibration of the second dipole stage. The data points are the measured position of a ^{13}N secondary beam for different values of magnetic rigidity. The line is a linear least–squares fit to the data, which was used in the energy calibration.

3.3.4 Horizontal Matrix Elements

A very important goal to be achieved regarding the horizontal coordinates is proper focusing of the beam on the position–sensitive silicon detector. While raytracing can in principle provide sufficient resolution even if the focus is not exactly on the detector, it is usually desirable to avoid this additional complication. Focusing was checked with the primary beam and a carbon reaction target at image No. 2, employing the ^{12}C(^{14}N,^{13}C)^{13}N reaction. The first dipole stage was tuned to produce a ^{14}N beam spot of minimal size on the reaction target ($\approx 0.5\,$mm), in an effort to ensure correct focusing. Due to the large angular width induced on the beam by the reaction, any possible remaining correlation of angle and position is washed out. The focusing condition of the second dipole stage can then be verified by plotting θ_f versus x_f, as shown in Fig. 3.8. The top part of that figure shows the A1200 focal–plane to be clearly out of focus, whereas the bottom part exhibits good focusing. The only adjustment between collecting the two spectra was a 4% increase of the "A061TA" quadrupole magnet, located right after the second pair of A1200 dipoles.

In order to obtain the scattering angular distribution from the coordinates measured at the focal plane, some of the matrix elements governing the optics between the reaction target at the dispersive image and the focal plane have to be determined. This was achieved by transporting the ^{13}N secondary beam through the A1200 with the entire device set to the same magnetic rigidity. Position and angle at the dispersive image, which are measured by two parallel–plate avalanche counters, were correlated with coordinates at the focal plane and the matrix elements could be determined.

When measuring these correlations, it is very important not to be misled by cross–correlations. For example, if the secondary beam is not focused properly on

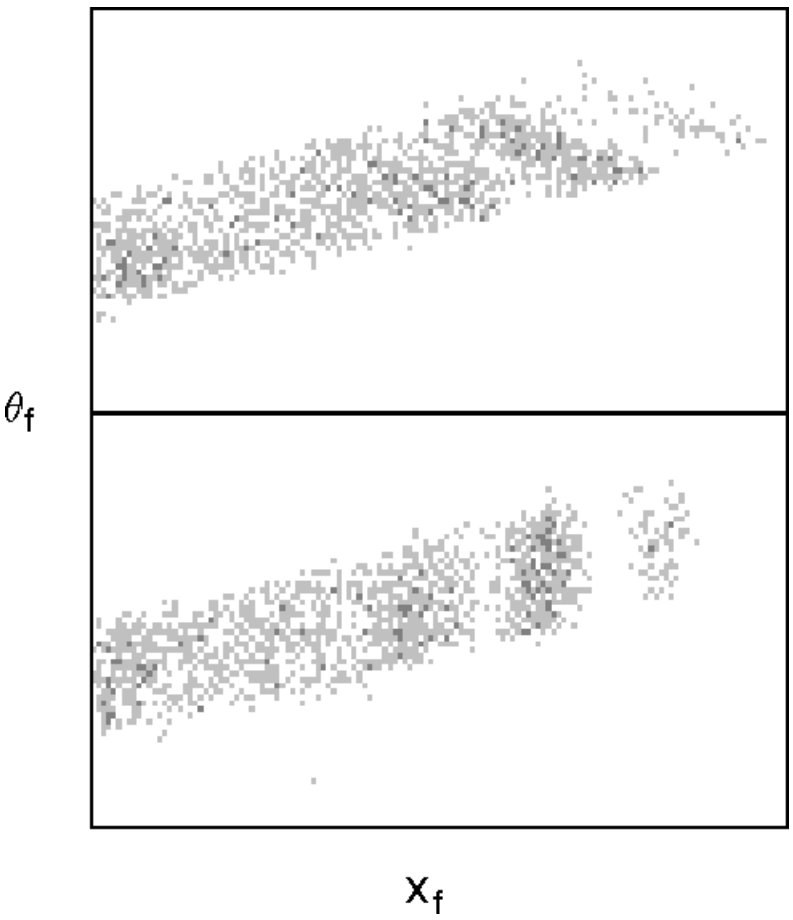

Figure 3.8: Focusing of the second A1200 dipole stage. Both spectra show a plot of θ_f vs. x_f for the $^{12}C(^{14}N,^{13}C)^{13}N$ reaction products. The ^{13}C phase space is dominated by the reaction, so that the focusing condition from the reaction target to the focal plane can easily be checked. The top spectrum shows a strong $(x|\theta)$ correlation, with the actual focus occurring downstream of the focal–plane detectors. The bottom spectrum, obtained after increasing the quadrupole field, shows that the focusing condition is fulfilled. *Scale: 60 mrad by 58 mm, top and bottom.*

the reaction target, but farther up– or downstream, the vertical position y_i at the reaction target will be correlated with angle ϕ_i. A plot of e.g. y_i versus the focal–plane coordinate y_f will then have built–in correlations with ϕ_i which will lead to erroneous results. This complication is avoided if a small cut in ϕ_i is imposed on the y_f versus y_i plot, ensuring that only the intrinsic dependencies are investigated. Other coordinates have to be treated likewise. Fig. 3.9 shows the spectrum used to determine the angular correlation $(\theta|\theta)$, with a cut in x_i imposed on the data. The line through the data represents the resulting matrix element $(\theta|\theta) = -0.65$.

3.3.5 Vertical Matrix Elements

Fig. 3.10 shows the correlation spectra used to determine the vertical first–order matrix elements. The position z_f at which y_f is calculated was varied to satisfy the condition $(y|y) = 0$. This corresponds to the intersection of the dashed line and the optical axis in Fig. 3.6 and is equivalent to the focal point in the the point–to–parallel mode. The lines through the data show the correlations determined from the spectra. The parameters that are of importance in calibrating the angular spectra are the matrix element $(y|\phi) = -0.022\,\mathrm{cm/mrad}$ and the coordinate $z_f = 78\,\mathrm{cm}$, upstream of the nominal focal–plane position.

There is the possibility, at least in principle, to exploit the unitarity condition in determining the matrix elements. For example, under the focusing condition $(x|\theta) = 0$, the determinant of the horizontal submatrix becomes

$$\begin{vmatrix} (x|x) & (x|\theta) \\ (\theta|x) & (\theta|\theta) \end{vmatrix} = \begin{vmatrix} (x|x) & 0 \\ (\theta|x) & (\theta|\theta) \end{vmatrix} = (x|x)\,(\theta|\theta) = 1. \tag{3.6}$$

However, the $(x|x)$ matrix element cannot be determined experimentally, since the beam spots are only marginally larger than the detector resolution. In the vertical coordinate, it was similarly found that the matrix element $(y|\phi)$ could be more reliably

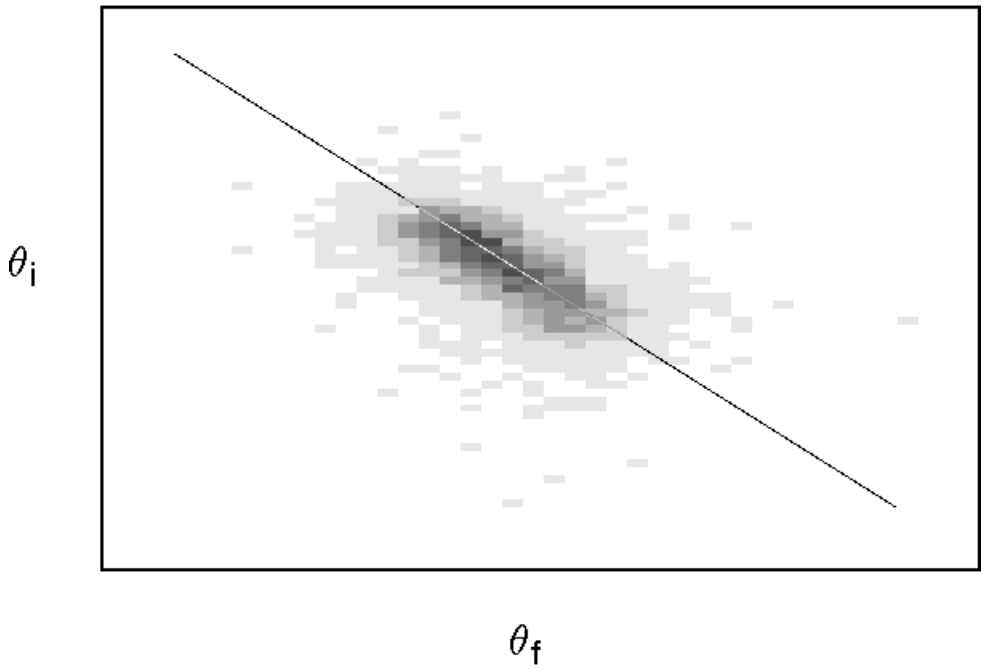

Figure 3.9: Determination of the $(\theta|\theta)$ matrix element. This spectrum was obtained with the ^{13}N secondary beam throughout the A1200 using position monitors both at the dispersive image and at the focal plane. A cut in horizontal position x_i has been imposed at the location of the reaction target. *Scale: 35 mrad by 20 mrad.*

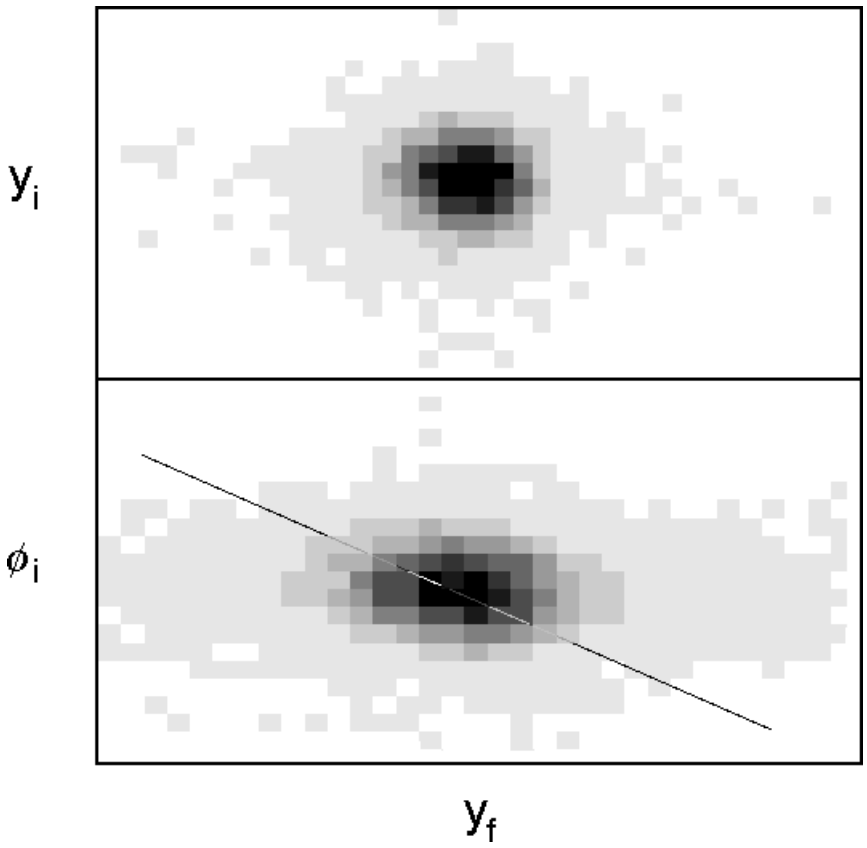

Figure 3.10: Spectra used to determine the vertical first–order matrix elements. The top spectrum shows a plot of y_i vs. y_f. The coordinate z_f at which y_f was calculated was varied until the $(y|y) = 0$ condition was reached. The bottom spectrum shows a plot of ϕ_i vs. y_f, recorded for the same z_f. The line through the data indicates the matrix element $(y|\phi)$. The beam was ^{13}N throughout the A1200, with position monitors at the dispersive image and the focal plane. *Scale: 8 mm by 14 mm (top), 20 mrad by 14 mm (bottom).*

determined from the data than its complement (ϕ|y).

3.3.6 Achromatism and Image Aberrations

While most first–order matrix elements can be determined off–line, some conditions are required to successully perform the experiments. As discussed in section 3.3.4, the imaging condition (x|θ) = 0 is convenient, but not absolutely essential, because raytracing can be used to improve the resolution in the data analysis. The most important optical property in reaction experiments is achromatism: (x|δ) = 0 and (θ|δ) = 0, applied to the entire device. The two dipole stages by themselves are, of course, dispersive. Since momentum measurements of the secondary beam cannot be performed due to the high incident rate during production runs, any deviation from (x|δ) = 0 will degrade the energy resolution. The achromatic condition can be checked by sending a limited rate of secondary–beam particles through the device and using the x_i coordinate as a measure of momentum, since x_i and δ_i are correlated by the dispersion of the first dipole stage.

Fig. 3.11 shows a x_i versus x_f plot obtained under those conditions. The data show that there is no first–order correlation between position at the focal plane and secondary–beam momentum, i.e. (x|δ) = 0. This spectrum was obtained as the result of several hours of tuning, with quadrupoles being adjusted to match the dispersions of the two dipole stages and sextupoles eliminating any 'banana' shapes of the curve. The hourglass shape of the data indicates higher–order image aberrations, which could not be eliminated with the available optical elements. An attempt was made to reproduce and understand this shape with the second–order computer code TURTLE [Car64], but was unsuccessfull, and the origin and nature of the aberrations are not fully understood. In an effort to balance count rate and resolution, the reaction target was cut to a smaller size, as indicated by the two horizontal lines in the figure, trading

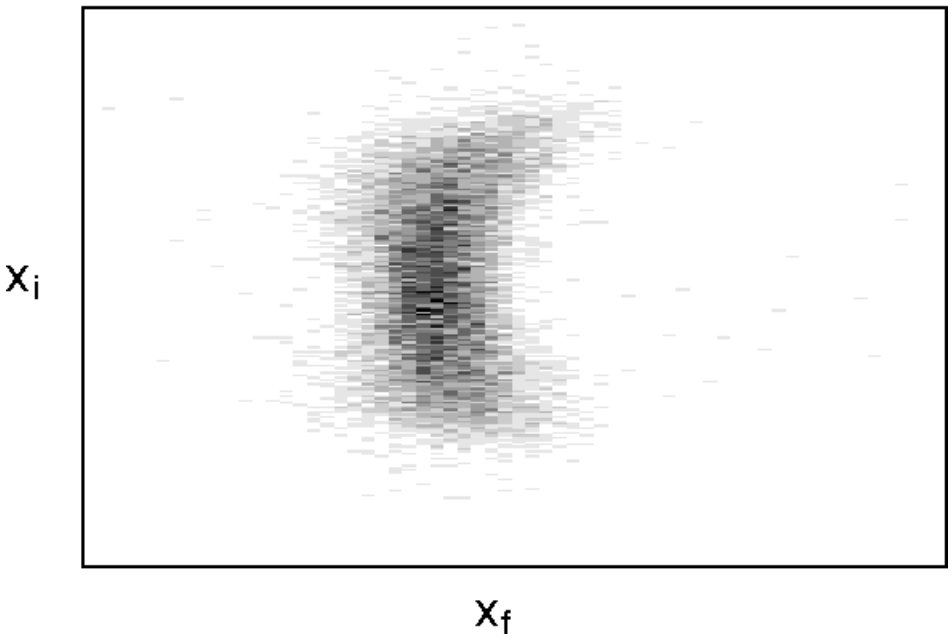

Figure 3.11: By plotting x_i vs. x_f for the ^{13}N secondary beam, the dispersion–matching condition can be checked. Since the horizontal beam spot size at the dispersive image is dominated by the momentum width of the secondary beam, dependence of position x_f at the focal plane on momentum can be determined. The general vertical trend of the data suggests first–order achromatism, but the overall asymmetric hourglass shape indicates higher–order aberrations. *Scale: 96 mm by 21 mm.*

about a third of the available secondary–beam intensity for a 20% improvement in resolution.

An example where image aberrations could be corrected with the available magnets is shown in Fig. 3.12, which shows a θ_f versus x_i plot for the $^{12}C(^{14}N,^{13}C)^{13}N$ reaction (compare with Fig. 3.8). The curved shape of the lines in the spectrum indicates a second–order aberration, which was corrected using the sextupole magnets of the second dipole stage. It is interesting to note that Fig. 3.12 is already an improvement over the initial situation, where the sextupole settings had incorrect polarity and the aberrations were so severe that the problem could not even be diagnosed from the spectrum.

3.3.7 Acceptance Correction

One of the technical difficulties associated with measuring the angular distribution of the the charge–exchange reaction products is the limited acceptance of the A1200. While the Reaction Mode offers significant sensitivity at fairly large scattering angles, the acceptance window is highly asymmetric, with a full width of about 20 mrad in θ_i and more than 40 mrad in ϕ_i. In order to convert the measured angular distribution of the reaction products, the acceptance for each scattering–angle bin has to be determined and divided out.

Acceptance was calculated with the beam–optics code TURTLE [Car64], which uses a Monte Carlo approach and the same underlying calculations as TRANSPORT. Input for the program were the known dimensions of the second A1200 dipole stage and magnetic–field settings calculated from the magnet currents, together with correction factors routinely used in applying TRANSPORT calculations to the A1200 magnets.

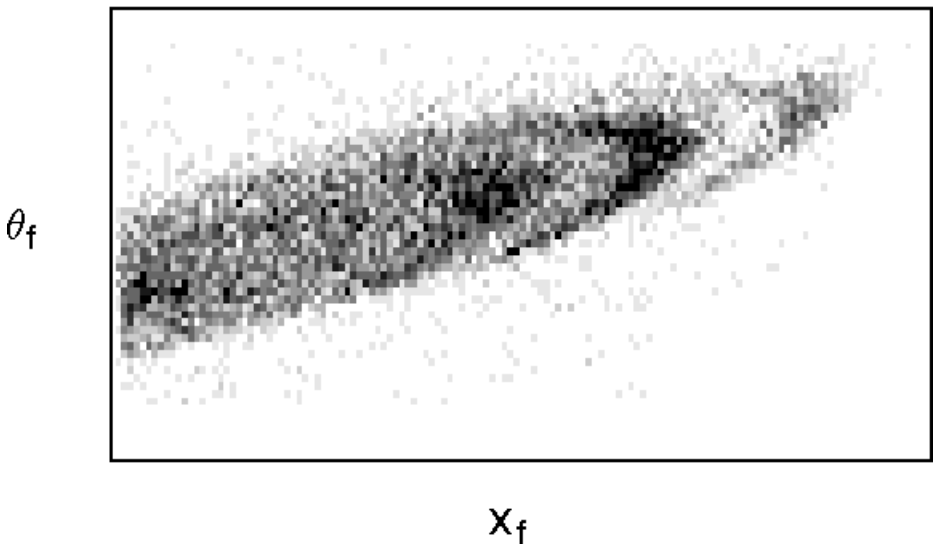

Figure 3.12: A plot of θ_f vs. x_f for products of the $^{12}C(^{14}N,^{13}C)^{13}N$ reaction. The spectrum is similar to Fig. 3.8, but the curved shape of the data suggests strong image aberrations, caused by faulty settings of the sextupole elements. *Scale: 50 mrad by 47 mm.*

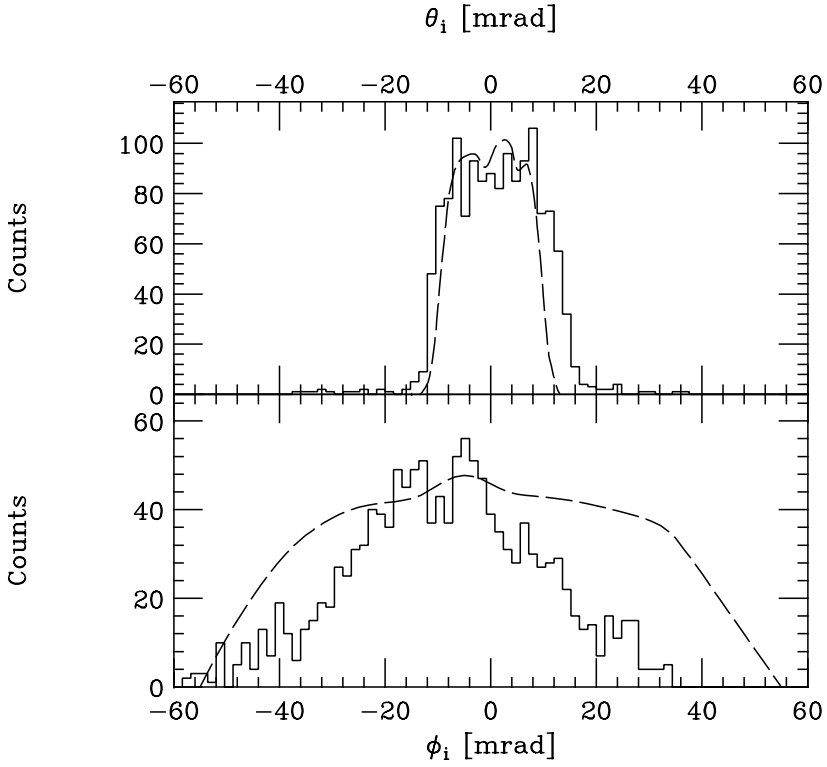

Figure 3.13: One–dimensional acceptance in the $\theta_{\rm i}$ and $\phi_{\rm i}$ coordinates. The histogram at the top shows the $\theta_{\rm i}$ spectrum for the ^{12}C(^{14}N,^{13}C)^{13}N reaction. The dashed line is the acceptance calculated with TURTLE and normalized to the data. The bottom figure shows the equivalent $\phi_{\rm i}$ curves.

Fig. 3.13 shows the result of a TURTLE calculation for the 57 MeV experiment using first– and second–order matrix elements. The histogram in the top part is the $\theta_{\rm i}$ distribution for the ^{12}C(^{14}N,^{13}C)^{13}N reaction products, which have an angular distribution wide enough to fill the aperture. Acceptance is determined by simulating a beam with a wide, rectangular–shaped angular distribution, originating at the reaction target. The calculation is done twice, once without apertures and once imposing realistic constraints on the physical size and shape of the beam pipe, quadrupoles, and dipoles. The ratio of count rate with and without aperture constraints for any given angle bin provides the acceptance. The TURTLE simulation, shown by the dashed line, fits the measured data quite well, which indicates the validity of the method. The lower portion of the figure shows the equivalent plot for the vertical coordinate. Obviously, the measured ϕ_i distribution is off–center with respect to the acceptance, which is the result of a misalignment of the secondary beam. This may have been caused by an error in the vertical position of the beam spot on the production target. Upon entering the quadrupole fields, such a shift will cause the beam to be deflected towards the optical axis, resulting in an angular misalignment. The angular width of the ^{13}C reaction products appears to be significantly smaller than the acceptance of the device.

In order to determine the acceptance for each scattering angle, a two–dimensional approach was used. Just as in the one–dimensional case, a wide beam was simulated, once with and once without aperture constraints. A two–dimensional histogram was developed, ranging from -20 to +20 mrad in $\theta_{\rm i}$ and from -60 to +60 mrad in $\phi_{\rm i}$, with bin sizes of 0.5 and 1 mrad, respectively. Simulated particles emerging from the reaction target were recorded in the appropriate bin, and the acceptance for each bin was determined. The coordinates of the secondary beam, $\theta_{\rm i}^0$ and $\phi_{\rm i}^0$, were then used

to convert the two–dimensional result to a one–dimensional scattering angle:

$$\theta_{\mathrm{scatter}} = \sqrt{(\theta_{\mathrm{i}} - \theta_{\mathrm{i}}^0)^2 + (\phi_{\mathrm{i}} - \phi_{\mathrm{i}}^0)^2}. \tag{3.7}$$

The result of this calculation is shown in Fig. 3.14, where the acceptance is plotted as a function of laboratory scattering angle. Due to the limited horizontal acceptance, there is a significant loss of particles for any angle larger than about 10 mrad. However, thanks to the vertical point–to–parallel focusing, there is significant acceptance beyond 40 mrad scattering angle.

Fig. 3.15 illustrates the process of acceptance correction: The solid line shows a Gaussian curve with a width similar to that obtained in the experiment (see chapter 5), and the full symbols show how this distribution is distorted by the limited spectrometer acceptance. During the data analysis, the measured differential cross section for each angular bin is divided by the corresponding acceptance value in order to obtain a realistic angular distribution. In the present example, this acceptance correction of course reproduces the original Gaussian, as shown by the open symbols.

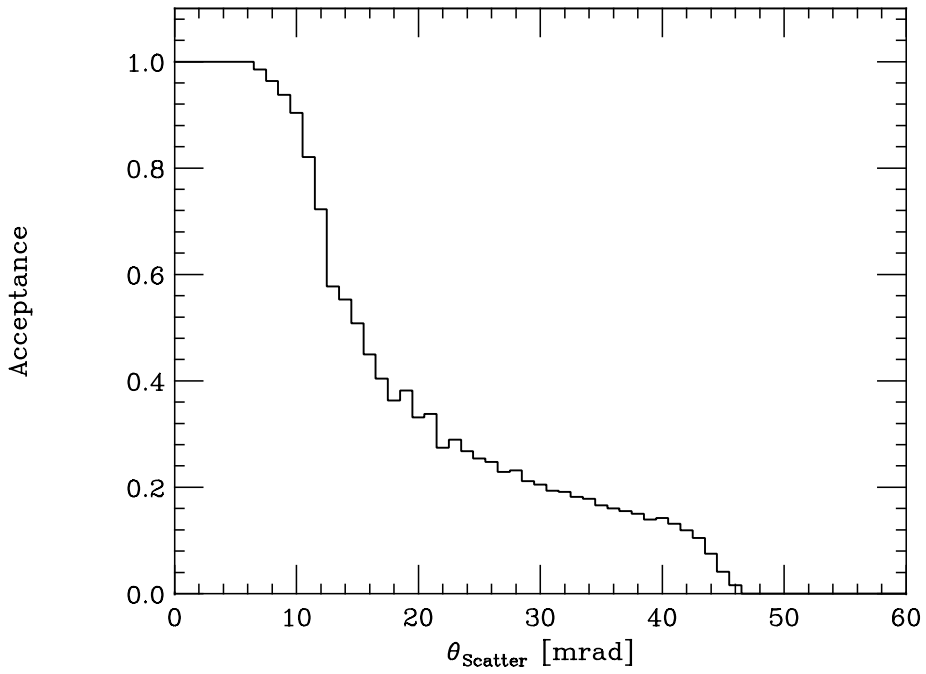

Figure 3.14: Acceptance as a function of scattering angle $\theta_{\mathrm{Scatter}}$. The curve shows the result of a TURTLE calculation, taking into account the coordinates of the ^{13}N secondary beam.

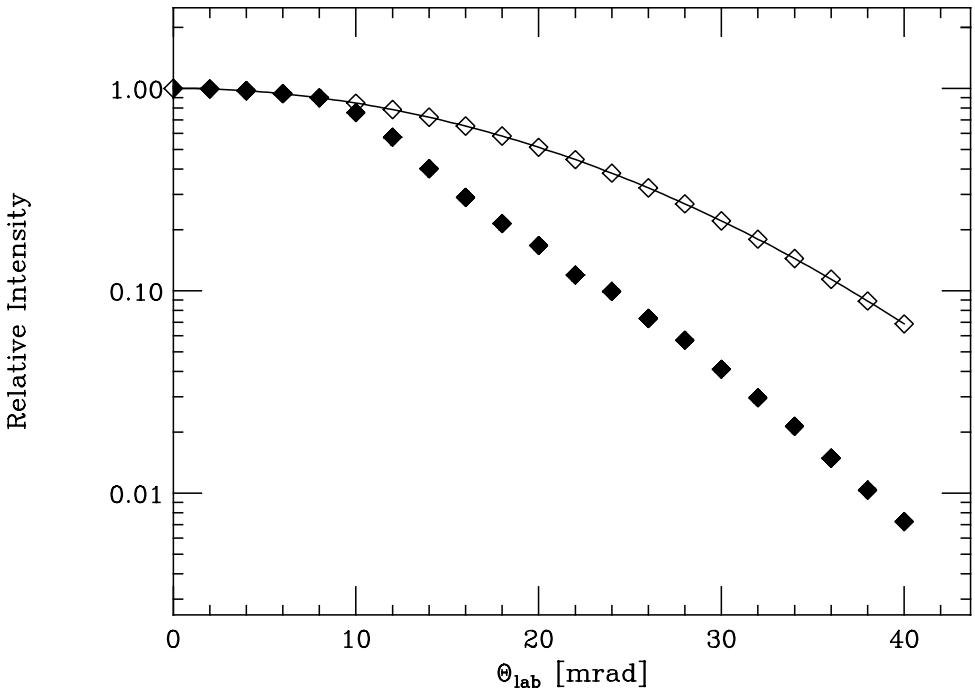

Figure 3.15: Acceptance correction of an angular distribution. The solid line is a Gaussian curve with a width similar to that observed experimentally. The full symbols represent the angular distribution that would be observed in the experiment, while the open symbols illustrate the effect of acceptance correction.

Chapter 4

Data Analysis

While some of the experimental parameters had to be determined on–line, others were left to the off–line data analysis. The following sections deal with the issues of determination of the background rate, total and differential cross sections, and unfolding of the angular distributions.

4.1 Background Determination

In the 57 MeV experiment, background was determined by replacing the ^{13}C target with a ^{12}C target of the same thickness and observing the ^{13}C ions at the focal plane. Because the Q value of the $^{12}C(^{13}N,^{13}C)^{12}N$ reaction is -15.1 MeV, the reaction products are displaced by 15 MeV on the excitation energy scale and do not contribute to the region of interest. Scattered beam particles, however, and fragmentation reactions of the ^{14}N primary beam are influenced little by the change in target, so that the observed ^{13}C spectrum should provide a good measure of the background rate.

The top panel of Fig. 4.1 shows the energy–calibrated focal–plane position spectrum of all data collected with the ^{13}C target. The counts observed at negative excitation energy are a clear indicator of background, since this region is energetically inaccessible to the $^{13}C(^{13}N,^{13}C)^{13}N$ reaction products. The center panel shows a

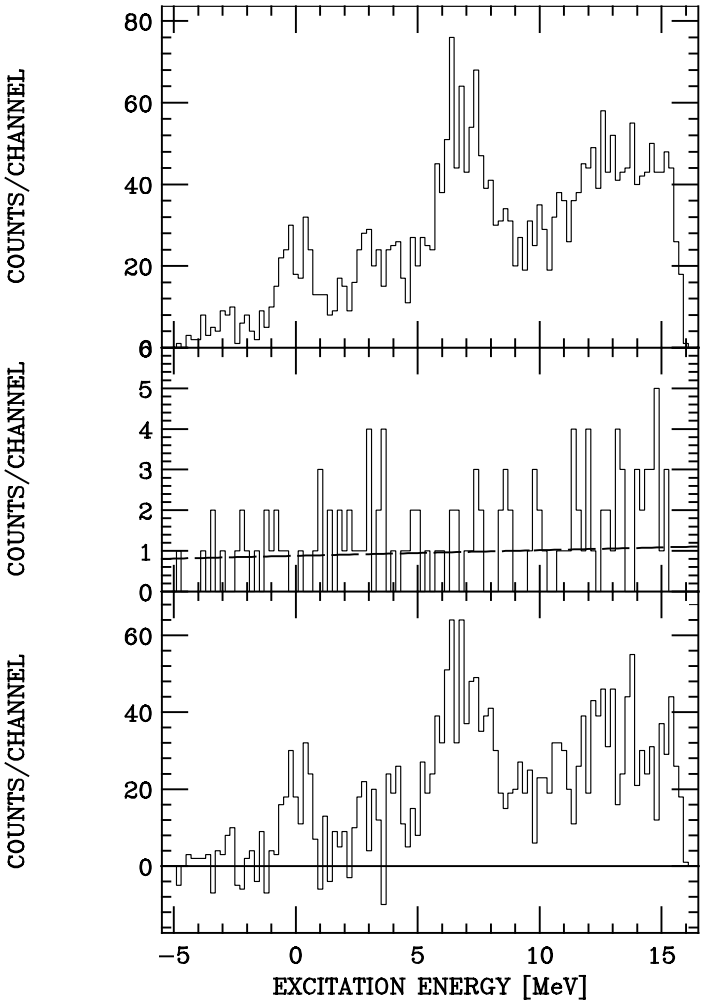

Figure 4.1: Background correction for the 57 MeV experiment. The top panel shows data collected with the ^{13}C target, the middle panel shows the result of a ^{12}C–target background run, and the bottom panel contains the background–corrected spectrum.

^{13}C spectrum collected over a period of six hours with the ^{12}C target. The count rate tends to increase towards higher excitation energy, but no peak structure is visible. At the bottom of Fig. 4.1 is the background–subtracted ^{13}C(^{13}N,^{13}C)^{13}N spectrum. It was obtained by multiplying the background spectrum by a factor of 6.2 to account for the difference in the amount of incident secondary–beam particles, and subtracting it from the ^{13}C(^{13}N,^{13}C) spectrum. While the result of this procedure is unsatisfactory due to the poor statistics involved, the average number of counts at negative excitation energy is close to zero, indicating the validity of the approach.

Instead of subtracting the spectra directly, the background was assumed to be smooth and the spectrum was fit with a first–order polynomial — shown by the dashed line in the center panel — which was used in the subtraction process.

A somewhat different approach was used for the 105 MeV experiment. It became apparent during the run that the background rate was correlated with the amount of scattered primary ^{14}N beam observed in the particle–identification spectrum. The ratio of ^{14}N to ^{13}N , which had been very stable during the 57 MeV experiment, ranged from approximately 0.7 to more than 6. The reason for this was most likely the fact that the target beam spot and the aperture limiting the angular acceptance of the A1200 were very close together. While that distance had been approximately 180 cm in the 57 MeV experiment, beam spot and slits were only 95 mm apart in the 105 MeV run, and the aperture was accordingly very small. A small change in the position of the beam spot could, therefore, have a large effect on the amount of scattered primary beam entering the device. The rate of counts observed in the negative excitation–energy region was high whenever the ^{14}N contamination was strong. In light of this behaviour, the approach used in the low–energy exeriment was considered insufficient, and the following analysis was performed instead:

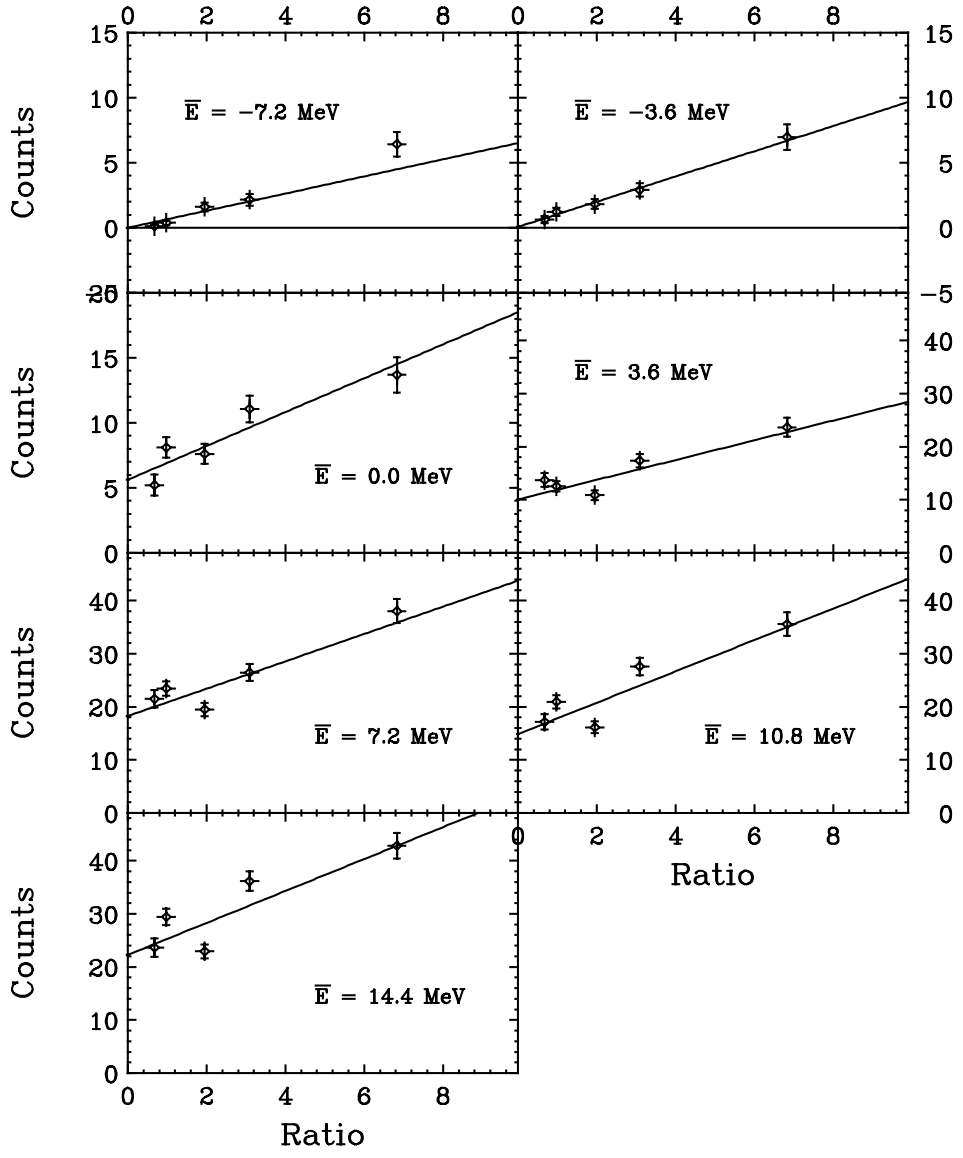

Figure 4.2: Background correction for the 105 MeV experiment. The top panel shows the excitation–energy spectrum, divided into bins for the background analysis. The six panels underneath show the normalized count rate as a function of contamination ratio for the first six energy bins.

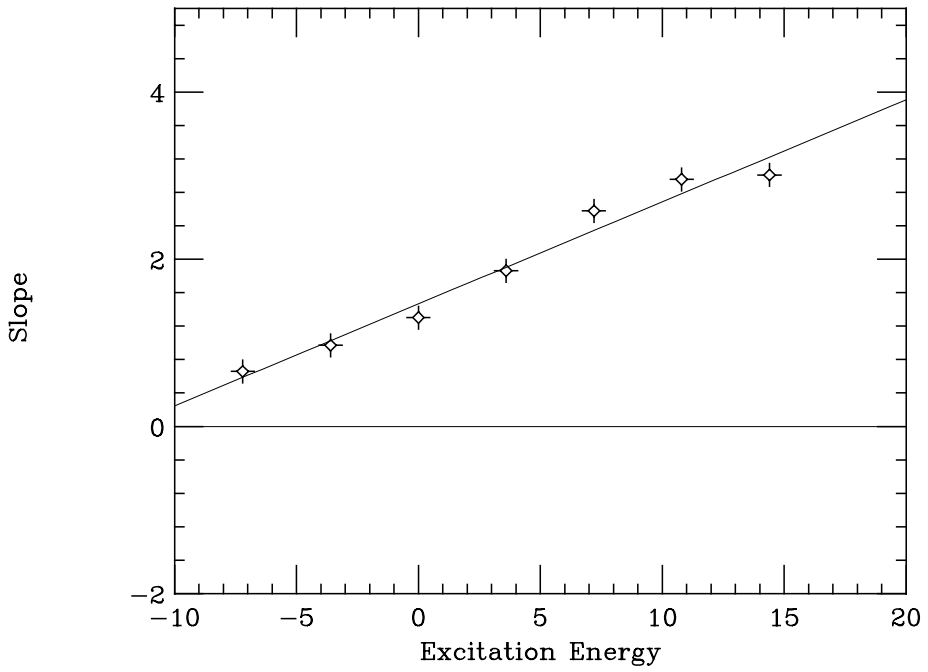

Figure 4.3: The slope parameters obtained for the seven energy bins, plotted as a function of the average energy of the bin. The line is the linear least–squares fit used in the final background subtraction.

- The excitation energy spectrum was divided equally into seven bins, 3.6 MeV wide each, and covering the region between -9.0 and +16.2 MeV.
- The available data files were divided into five groups, according to their $^{14}N/^{13}N$ contamination ratio.
- For each energy bin, the count rate, normalized to the intensity of the incident beam, was plotted as a function of contamination ratio, as shown in Fig. 4.2.
- The data were fit by first–order polynomials. The intersection of the curve with the y axis indicates the ^{13}C rate at zero contamination. Note that this value is close to zero for the two lowest–energy bins.
- The slope of the curve determines the background rate as a function of contamination. The slope values were plotted as a function of excitation energy, as shown in Fig. 4.3. In order to obtain a function varying smoothly with energy, a linear least–squares fit was performed, as indicated by the solid line.

The parameters of the fit, together with the observed numbers of ^{14}N and ^{13}N ions, was then used to perform a background subtraction similar to that described above for the low–energy experiment. The background–subtracted 105 MeV spectrum is shown in Fig. 3.2. Again, the average number of counts for negative excitation energy is compatible with zero.

4.2 Drifts

Each of the mirror charge–exchange experiments lasted just over a week, and several of the experimental observables exhibited a slow variation over time. Most notably, the position of the primary beam spot on the production target moved horizontally by up to a millimeter, probably due to variations in the cyclotron operating conditions.

Since the position at the A1200 focal plane is a real image of the initial beam spot, this behaviour caused the overall energy resolution to deteriorate significantly. Other observables, such as the total–energy signals from the plastic scintillator that stopped the ions, also exhibited slow variations with time, likely as a result of changing ambient temperature.

During A1200 experiments, data taking is routinely interrupted every two hours, and a new file is opened. Since the typical time scale of the variations were significantly longer than two hours, the problem was solved by determining the average value of the observables for the $^{13}N^{6+}$ ions and recalibrating the position, total–energy, and other signals relative to these values for each file. This procedure restored the original resolution almost completely.

4.3 Energy Spectra

The bottom panels of Fig. 4.4 show the background–subtracted, energy–calibrated position spectra for the $^{13}C(^{13}N,^{13}C)^{13}N$ reaction products. Three peaks are visible, at excitation energies of approximately 0 MeV, 3.5 MeV, and 7 MeV, plus a broader background structure above 10 MeV. The insets show the $^{13}N^{6+}$ position spectra, which were used for the absolute calibration of the energy scales. The peaks are slightly shifted from 0 MeV because of the differential energy loss in the reaction target.

To understand the structure, it is instructive to consider Fig. 4.5. On the assumption that the reaction proceeds primarily via single–step charge exchange, possible candidates for final states in the ejectile are the $J^\pi = 1/2^-$ ground state and the $3/2^-$ excited state at 3.68 MeV. The neutron–emission threshold of ^{13}C is at 4.95 MeV. Possible states in the target residue are the ground state, the $3/2^-$ state at 3.50 MeV,

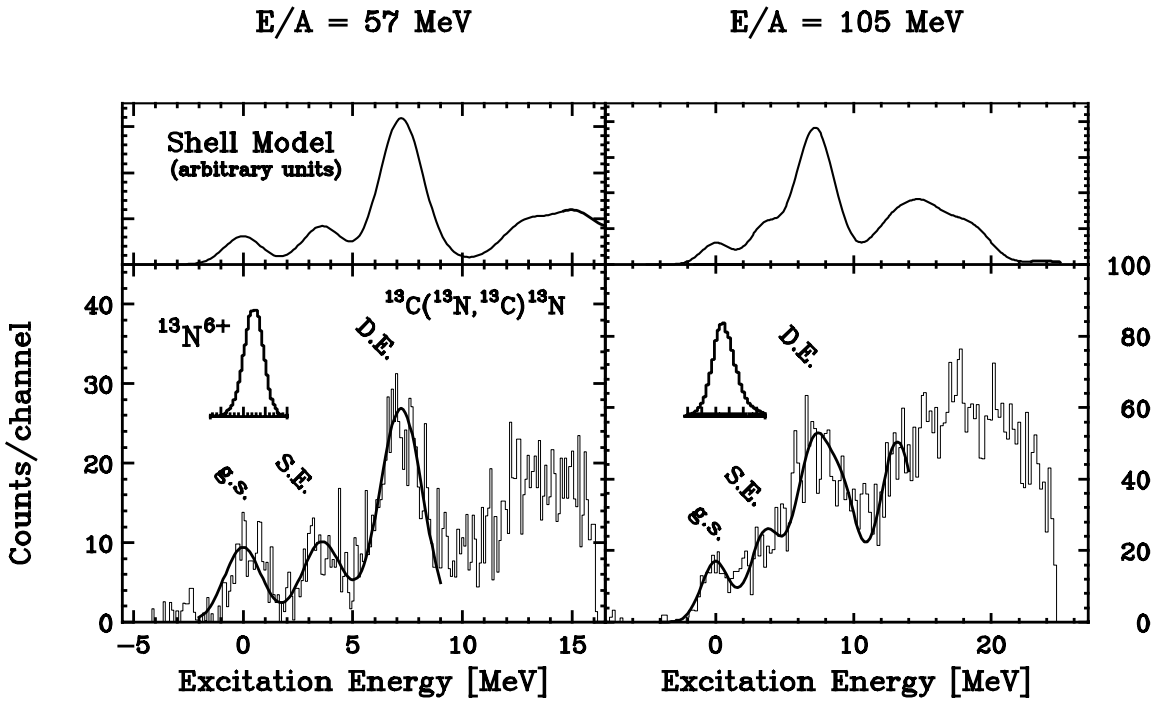

Figure 4.4: Energy specta and their interpretation. The histograms in the bottom panels show the background–corrected ^{13}C excitation–energy spectra, and the full lines are the fits described in the text. The insets show the $^{13}N^{6+}$ charge state peaks, and the top panels contain the results of shell–model calculations.

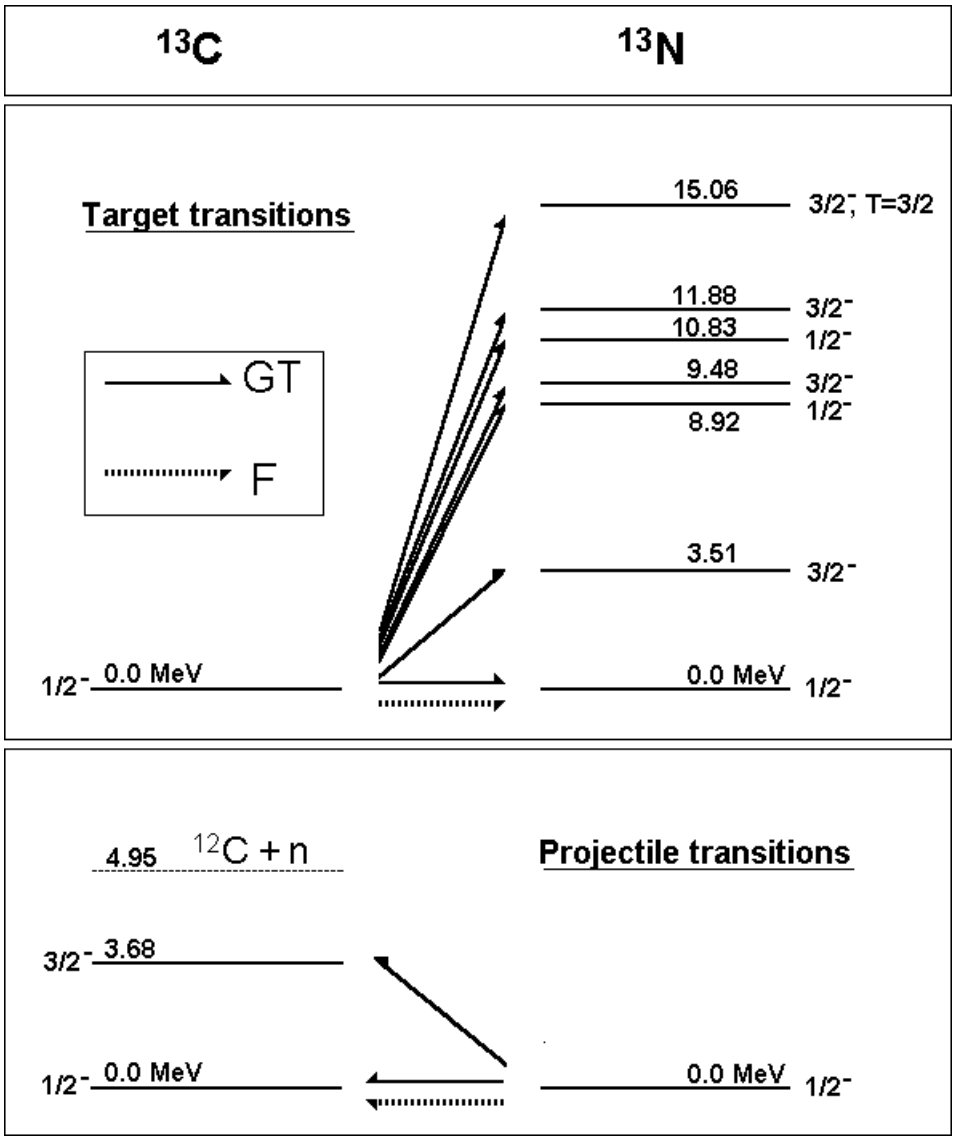

Figure 4.5: Schematic illustration of the target and projectile transitions in the ^{13}C(^{13}N,^{13}C)^{13}N reaction. Since the ejectile is detected in the reaction, only transitions to particle–stable states contribute to the observed cross section. There can be no cross–coupling of Fermi and GT–type transitions.

and further negative–parity states above 9 MeV of excitation energy. The transitions depicted in Fig. 4.5 were obtained from Mildenberger's analysis of 200 MeV ^{13}C(p,n) data [MiA91].

Since the one–step reaction can proceed either via a Fermi or via a GT transition, there can be no F/GT cross terms. Accordingly, the observed strength above the g.s. peak is entirely GT in nature, while the ground state is mixed.

For the analysis, only the three lowest resolved states were taken into consideration. The energy spectra were fit with multiple Gaussian curves of fixed positions and widths, with the peak area as the free parameter. For the 57 MeV experiment, three peaks were considered sufficient to describe the data: a) Ground state (g.s.): Both ejectile and target residue are in their ground states, b) Single Excitation (S.E.): The target residue is in the $1/2^-$ ground state and the ejectile in the $3/2^-$ state, or vice versa; c) Double Excitation (D.E.): Both nuclei are in the $3/2^-$ state. For the 105 MeV experiment, higher excitations were also allowed in the fit in order to obtain a reliable measure for the area under the D.E. peak. The results are shown by the solid lines.

The curves in the top panels of Fig. 4.4 were produced by assuming strict proportionality of the cross section to transition strength. GT strengths obtained from a shell–model calculation [ChB93] were multiplied by the experimentally determined unit cross section (see Chapter 5) and convoluted with the observed energy resolution. The double excitation peak at 7.2 MeV is overpredicted relative to the experiment, but this a result of the "^{13}C controversy" discussed in Section 2.3: The unit cross sections were determined assuming $B(GT)_{3/2^-} = 0.83$, while the shell–model calculation predicts $B(GT)_{3/2^-} = 2.38$. Aside from this built–in deviation, the shape of the spectra is reproduced remarkably well.

Table 4.1: Integrated cross sections determined from fitting the excitation energy spectra.

^{13}N Energy	E/A=57 MeV	E/A=105 MeV
$^{13}C_{g.s.}\sigma$	$31 \pm 4\,\mu$b	$15 \pm 2\,\mu$b
$^{13}C_{S.E.}\sigma$	$36 \pm 4\,\mu$b	$23 \pm 2\,\mu$b
$^{13}C_{D.E.}\sigma$	$102 \pm 6\,\mu$b	$59 \pm 4\,\mu$b

An unusual feature of the energy fits should be pointed out: Upon close inspection, the E/A = 57 MeV g.s. peak appears to be shifted up in excitation energy by 200 to 300 keV. While it is conceivable that this shift could be caused by an error in the determination of the zero of the energy spectrum, the fit to the double–excitation peak at 7.2 MeV is excellent. It seems rather unlikely that errors were committed in the determination of both the absolute value and the slope of the energy calibration in such a way as to cancel each other out near 7 MeV. No explanation has been found for this effect, but it should be noted that the area of the g.s. peak appears to be well reproduced by the fit and did not change appreciably when the peak position was allowed to vary. The problem was not investigated further. The E/A = 105 MeV data do not exhibit this kind of complication.

The integrated reaction cross sections, determined from the number of counts observed in each peak, are given in Table 4.3. In order to determine the forward cross sections $d\sigma/d\Omega(0^\circ)$, the angular distributions of the reaction products were determined for the three excitation–energy peaks in each experiment.

4.4 Angular Distributions

As outlined in Ch. [3], the horizontal and vertical angles θ_i and ϕ_i were determined from measurements of the two–dimensional particle position and angle at the focal

plane, after careful calibration of the first–order ion–optical properties of the second A1200 dipole stage. The $^{13}N^{6+}$ ions were used to define the θ_i=0 and ϕ_i=0 coordinates. The scattering angle was then determined from the relation

$$\theta_{\rm scatter} = \sqrt{(\theta_i - \theta_{^{13}N})^2 + (\phi_i - \phi_{^{13}N})^2}, \tag{4.1}$$

and histograms for the number of counts per scattering–angle bin — in the laboratory (lab) system — were obtained. These were converted to units of counts per msr of solid angle in the center–of–mass (c.m.) system. Due to the symmetry of the reaction, the relationship between lab and c.m. angle is a very simple one to first approximation: $\theta_{\rm c.m.} = 2 \times \theta_{\rm lab}$. The difference in mass between ^{13}C and ^{13}N is 2.22 MeV/c^2 and is ignored, but relativistic effects are more important, and the actual conversion factors between $\theta_{\rm c.m.}$ and θ_{lab} are 2.030 (2.053) for E/A = 57 MeV (105 MeV).

Fig. 4.6 illustrates this process. The top panel shows the energy–calibrated position distribution of ^{13}C ions at the focal plane for the E/A=57 MeV experiment. A software cut is used to select the $^{13}C_{g.s.}$ reaction products, as indicated by the two vertical lines. The center panel shows the $\theta_{\rm lab}$ histogram for the selected particles. The bottom panel shows the same data, but converted to units of counts/msr. The axes for the angle spectra were chosen to be equivalent in order to facilitate comparison, and the error bars represent the statistical uncertainty only. Once the spectrum is corrected for the spectrometer acceptance, a realistic angular distribution is obtained. However, care must be taken with the normalization of the data.

Firstly, the number of counts for which angular coordinates could be obtained are limited by the efficiency of the focal–plane position monitors. While this detector efficiency was close to 100% for the CRDCs used in the 105 MeV experiment, it was only approximately 65% for the 57 MeV experiment, where PPACs were used. Secondly, the software cuts imposed on excitation energy are sufficient to determine the shape

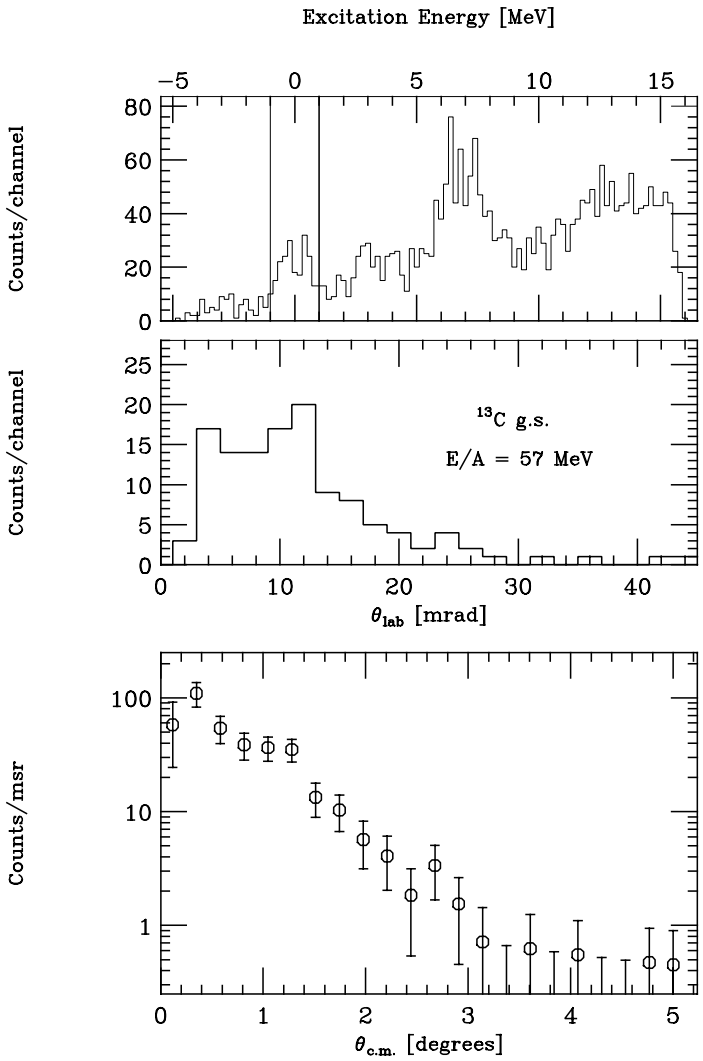

Figure 4.6: Scattering–angle analysis, shown for the E/A=57 MeV ^{13}C ground state as an example. The middle panel shows a scattering–angle histogram for the data selected by the software cut in the top panel. The same data are displayed at the bottom after conversion to units of counts per c.m. solid angle. No acceptance correction was performed, and the scales of the x axes in the two lower panels are equivalent. The error bars represent the statistical uncertainty only.

Table 4.2: Fit parameters for the angular distributions

E/A = 57 MeV			
	Maximum	rms width (c.m.)	χ^2
$^{13}N^{6+}$	—	0.52°	24
^{13}C ground state	63±6 msr^{-1}	1.16°	0.67
^{13}C single excitation	56±5 msr^{-1}	1.43°	1.73
^{13}C double excitation	133±8 msr^{-1}	1.42°	1.29
E/A = 105 MeV			
	Maximum	rms width (c.m.)	χ^2
$^{13}N^{6+}$	—	0.50°	78
^{13}C ground state	190±14 msr^{-1}	0.85°	0.96
^{13}C single excitation	294±17 msr^{-1}	0.92°	1.36
^{13}C double excitation	533±22 msr^{-1}	0.91°	1.00

of the angular distribution, but do not accurately reflect the number of counts in the peak, which has to be determined by peak fitting. Lastly, the widths of the measured angular distributions are not solely due to the charge–exchange reaction process, but also in part to the width of the secondary beam, which has to be deconvoluted from the measured distributions.

The following procedure was used in determining the forward cross section. For all peaks, the acceptance–corrected angular distribution was determined in units of counts per msr. The peak value, $dN/d\Omega(0^o)$, was determined by fitting the data with a Gaussian curve, with the peak width and area as free parameters, and the centroid fixed at 0°. This procedure is empirically justified by the fact that the data are rather well reproduced, as indicated by the χ^2 values in Table 4.4. Furthermore, the angular distribution for single–step charge exchange obtained from a model calculation in eikonal approximation [Ber93] show a similar functional behavior for the $^{13}C(^{13}N,^{13}C)^{13}N$ cross section at small angles. The angular distributions obtained for both experiments are displayed in Fig. 4.7. The top panels show the angular

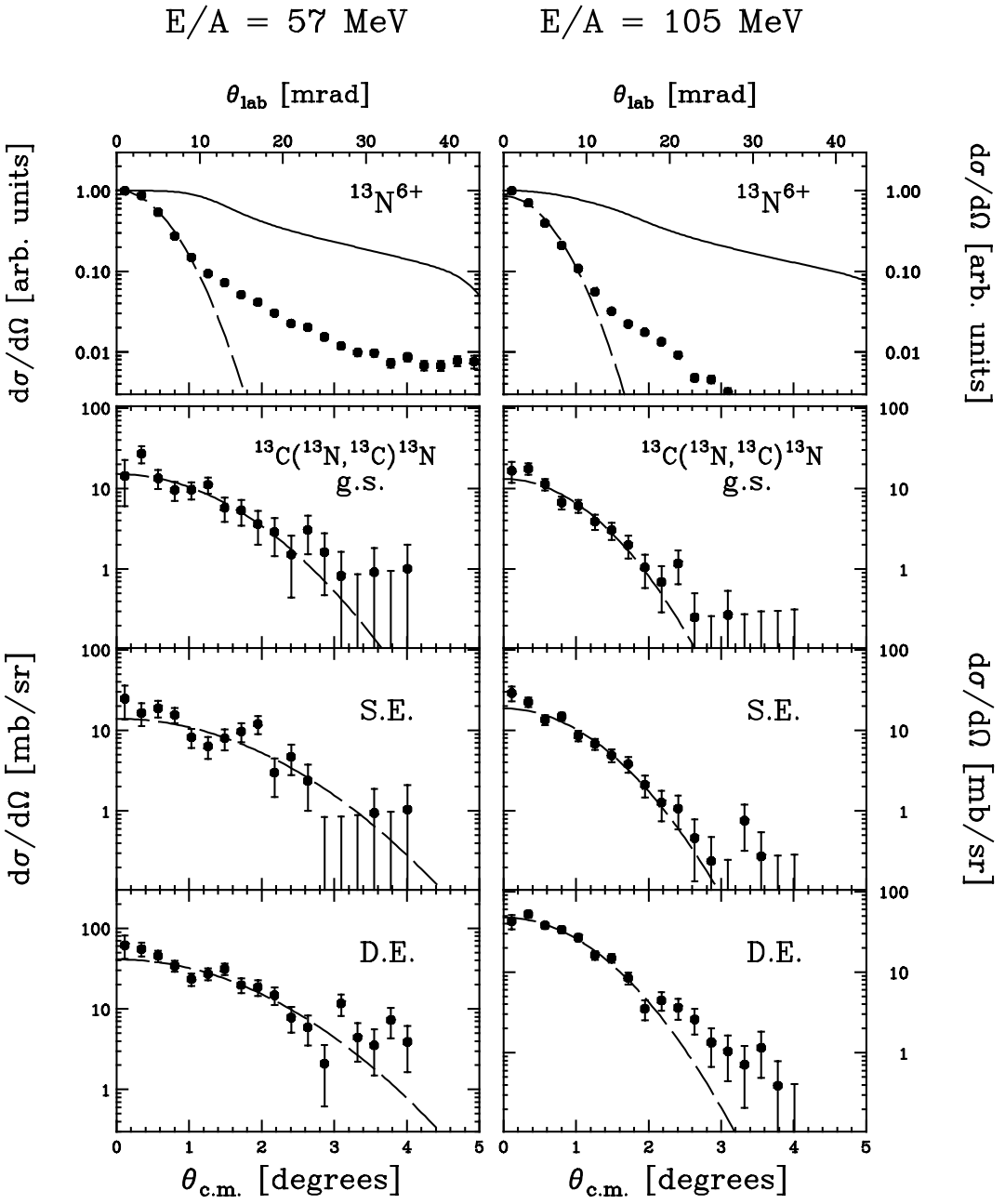

Figure 4.7: Angular distributions for the ^{13}N secondary beam, obtained from the 6+ charge state, and the three lowest peaks in the excitation–energy spectra.

Table 4.3: Results from the mirror charge–exchange experiments. The forward cross sections $d\sigma/d\Omega(0^\circ)$ were obtained through the procedure described in the text.

^{13}N Energy	E/A=57 MeV	E/A=105 MeV
$^{13}C_{g.s.}$ $d\sigma/d\Omega(0^\circ)$	17 ± 3 mb/sr	16 ± 3 mb/sr
$^{13}C_{S.E.}$ $d\sigma/d\Omega(0^\circ)$	15 ± 3 mb/sr	22 ± 4 mb/sr
$^{13}C_{D.E.}$ $d\sigma/d\Omega(0^\circ)$	44 ± 8 mb/sr	56 ± 10 mb/sr

distributions for the $^{13}N^{6+}$ secondary–beam. The solid lines depict the spectrometer acceptance, calculated with a modified version of the computer code TURTLE (see chapter 3). The curves are slightly different for the two experiments because of an improved optical solution employed in the 105 MeV experiment. The dashed lines show the results of non–linear least–squares Gaussian fits, limited to data at c.m. angles $\leq 1^\circ$. While the fits fail to account for the tails in the spectra, they describe the $^{13}N^{6+}$ data rather well down to 10% of the maxima, and were considered sufficient to use in unfolding the measured angular distributions. The angular distributions for the ground–state, single–excitation, and double–excitation peaks are shown in the six lower panels. After fitting, the spectra have been calibrated in units of mb/sr, The dashed lines show the results of Gaussian fits, limited to center–of–mass angles $\leq$ 2.4° (2.0°) for the 57 MeV (105 MeV) data. Parameters of the fits are given in Table 4.4. The final results for the forward cross sections were obtained from the following relation:

$$\frac{d\sigma}{d\Omega}(0^\circ) = \mathrm{Fit}(0^\circ) \times \mathrm{C} \times \frac{\Sigma \mathrm{E}^*}{\Sigma\theta_{\mathrm{scatter}}} \times \frac{\sigma}{\sqrt{\sigma^2 - \sigma_0^2}}, \tag{4.2}$$

where $\mathrm{Fit}(0^\circ)$ is the peak value of the fit to the angular distribution, C is a factor that converts the number of counts to units of millibarn, $\Sigma \mathrm{E}^*$ is the number of counts obtained from the fit to the excitation energy, and $\Sigma\theta_{\mathrm{scatter}}$ is the number of counts in the angular–distribution spectrum. The final correction applied accounts for the

finite resolution (σ_0) of the secondary ^{13}N beam, which is subtracted in quadrature from σ, the width of the ^{13}C reaction products. The resulting increase in the forward cross sections is relatively small — typically between 10 and 20% — which justifies the approximation of the ^{13}N distributions by a simple Gaussian. The results of this analysis are listed in Table 4.4.

Chapter 5

Results

As outlined in chapter 2, the relationship of zero–degree cross section to target transition strength for (p,n) reactions is conventionally written as:

$$\mathrm{d}\sigma/\mathrm{d}\Omega(0^{\mathrm{o}}) = \hat{\sigma}_{\mathrm{F}}\mathrm{F}(\mathrm{q},\omega)\mathrm{B}(\mathrm{F}) + \hat{\sigma}_{\mathrm{GT}}\mathrm{F}(\mathrm{q},\omega)\mathrm{B}(\mathrm{GT}), \tag{5.1}$$

This formula, which connects the charge–exchange cross section with the weak–interaction strength in the target only, is practical in the nucleonic case. It is not useful, however, for a description of heavy–ion charge exchange, especially in cases where the ejectile may be excited as well. Consider the present case: the physics of the interaction process clearly depends as much on the structure of the projectile nucleus as it does on the target structure.

Therefore, a more general form of equation 5.1 is proposed, which is physically better justified and will allow meaningful comparison of CEX data obtained with different systems:

$$\mathrm{d}\sigma/\mathrm{d}\Omega(0^{\mathrm{o}}) = \sigma^{*}_{\mathrm{F}}\mathrm{F}(\mathrm{q},\omega)\mathrm{B}(\mathrm{F})_{\mathrm{P}}\mathrm{B}(\mathrm{F})_{\mathrm{T}} + \sigma^{*}_{\mathrm{GT}}\mathrm{F}(\mathrm{q},\omega)\mathrm{B}(\mathrm{GT})_{\mathrm{P}}\mathrm{B}(\mathrm{GT})_{\mathrm{T}}, \tag{5.2}$$

where the transition strengths in both projectile (P) and target (T) are taken into account, and σ^{*} replaces $\hat{\sigma}$. The latter is only defined for the (p,n) reaction, in which case $\sigma^{*}_{\mathrm{F}} = \hat{\sigma}_{\mathrm{F}}$ and $\sigma^{*}_{\mathrm{GT}} = \frac{1}{3}\,\hat{\sigma}_{\mathrm{GT}}$, since B(F) = 1 and B(GT) = 3. In the present case,

$Q_{gs} = 0$, and the correction factor $F(q,\omega)$ is estimated from the systematics outlined in Ref. [TaG87] to be greater than 0.95 (0.98) for the 57 MeV (105 MeV). It will be dropped from the equations and is not considered further.

Using equation 5.2, the cross section of the three peaks in the energy spectra, and the structural symmetry of the mirror nuclei, the following equations are derived:

$$d\sigma/d\Omega(0^o)_{g.s.} = \sigma_F^* B(F)^2_{1/2^-} + \sigma_{GT}^* B(GT)^2_{1/2^-} \tag{5.3}$$

$$d\sigma/d\Omega(0^o)_{S.E.} = 2\sigma_{GT}^* B(GT)_{1/2^-} B(GT)_{3/2^-} \tag{5.4}$$

$$d\sigma/d\Omega(0^o)_{D.E.} = \sigma_{GT}^* B(GT)^2_{3/2^-}. \tag{5.5}$$

There is no mixing of Fermi and GT–type transitions, since the interaction is presumed to be one–step in nature. Note that the possibility of ejectile excitations gives rise to three peaks instead of the two obtained in nucleon–induced charge exchange. From the resulting three equations 5.3–5.5, it is in principle possible to extract the unknowns $\hat{\sigma}_F$ and $\hat{\sigma}_{GT}$, as well as $B(GT)_{3/2^-}$, which is not available from β–decay measurements.[1] However, this requires reliance on the assumption of specific proportionality, which has been called in question for ^{13}C.

Given the uncertainty regarding ^{13}C(p,n), it is considered a better choice to use the (p,n) results of Ref. [RaW87] for and to draw conclusions based on a comparison between the HICEX and (p,n) studies.

Using the measured cross sections, $B(F)_{1/2^-} = N - Z = 1$, and the literature values $B(GT)_{1/2^-} = 0.200 \pm 0.004$ (from β–decay) and $B(GT)_{3/2^-} = 0.83 \pm 0.03$ [from the (p,n) reaction] [RaW87], equations 5.3–5.5 can be solved to yield values for σ_F^* and σ_{GT}^*. The results are given in Table 5.1. For comparison, experimental results obtained for ^{13}C targets with beams of protons and ^3He are also included

[1] This analysis results in $B(GT)_{3/2^-} = 1.2 \pm 0.3$ (1.0 ± 0.2) for the E/A = 57 MeV (100 MeV) experiment, right between the Goodman/Watson results of 0.83/1.38.

Table 5.1: Unit cross sections obtained in the mirror charge–exchange experiments. The extraction of these parameters is based on results from the ^{13}C(p,n) reaction.

^{13}N Energy	E/A=57 MeV	E/A=105 MeV
$\sigma_{\rm F}^*$	15 ±2 mb/sr	13 ±2 mb/sr
$\sigma_{\rm GT}^*$	55 ±10 mb/sr	74 ±13 mb/sr
Other Results:	(^{3}He,t) E/A=67MeV	(p,n) E=160 MeV
$\sigma_{\rm F}^*$	5.5±0.5 mb/sr	1.6±0.3 mb/sr
$\sigma_{\rm GT}^*$	4.1±0.2 mb/sr	4.2±1.2 mb/sr

[RaW87, JäB94].

The specific cross sections found for the present case are surprisingly large, and $\sigma_{\rm GT}^*$ shows a small increase with increasing energy, while $\sigma_{\rm F}^*$ decreases slightly.

A model calculation [Ber93] for the ^{13}C(^{13}N,^{13}C)^{13}N reaction at E/A=70 MeV predicts 3.5 mb/sr for the GT part of the forward g.s. cross section. The experimental value, determined from the E/A = 57 MeV σ^* and relation 5.3, is 2.2 ± 0.4 mb/sr. This calculation is based on a relatively simple eikonal approximation and employs harmonic–oscillator wave functions, so that the expected accuracy is less than a factor of two. It should be noted that the theoretical prediction implies $\hat{\sigma}^* = 87.5$ mb/sr, which is larger still than the experimentally obtained values. Given the level of sophistication of the model, the results are surpisingly close to the experimental ones.

The increase in cross section with bombarding energy is in contrast with (p,n) charge exchange, where $\sigma_{\rm GT}^*$ remains unchanged, while $\sigma_{\rm F}^*$ decreases with energy [TaG87]. In ^{12}C(^{12}C,^{12}N)^{12}B HICEX, however, an increase in GT cross section has been observed, with values for $\sigma_{\rm GT}^*$ of 5.4 mb/sr (17 mb/sr) at E/A = 70 MeV (135 MeV) [AnW91, IcI94]. As outlined in section 2.4, the increase in cross section is attributed to enhanced nuclear transparency at increased bombarding energy.

A test of proportionality that is independent of calibration is obtained by com-

bining Eqs. 5.4 and 5.5:

$$\frac{\mathrm{d}\sigma/\mathrm{d}\Omega(0^{\circ})_{\mathrm{D.E.}}}{\mathrm{d}\sigma/\mathrm{d}\Omega(0^{\circ})_{\mathrm{S.E.}}} = \frac{\mathrm{B(GT)}_{3/2^-}}{2\,\mathrm{B(GT)}_{1/2^-}}. \tag{5.6}$$

The experimentally obtained values for the left–hand side of Eq. (6) are 2.9 ± 0.5 (2.5 ± 0.7) for the 57 MeV (105 MeV) experiment, in fair agreement with the right–hand–side value of 2.08 ± 0.09.

For further comparison, the values of $\sigma^*_{\mathrm{GT}}/\sigma^*_{\mathrm{F}}$ as a function of energy for the three charge–exchange reactions ^{13}C(p,n)^{13}N [TaG87, RaW87, Rap95], ^{13}C(^{3}He,t)^{13}N [JäB94, AkD94], and ^{13}C(^{13}N,^{13}C)^{13}N are shown in Fig. 5.1. The data indicate that $\sigma^*_{\mathrm{GT}}/\sigma^*_{\mathrm{F}}$ increases with projectile mass. This increase is attributed to the strong absorption in heavy–ion reactions, which selects large impact parameters and therefore emphasizes the longest–range part of the nuclear force. The spin–flip part of the interaction is mediated by single pion exchange and hence is enhanced with respect to the non–spin–flip portion, which has the shorter–range characteristics of multiple pion exchange.

In summary, the results obtained in this study indicate that HICEX can be used for weak–interaction studies in much the same way as the (p,n) reaction. The experimental energy spectra can be understood in terms of weak–interaction strengths in both projectile and target. However, the large specific cross sections obtained for (^{13}N,^{13}C) mirror charge exchange, as well as the unexpectedly large ratio of GT to Fermi unit cross section, underscore the need for a reliable calibration procedure. With only a few systems studied so far, much further experimental work is necessary to understand the physics involved in the HICEX process.

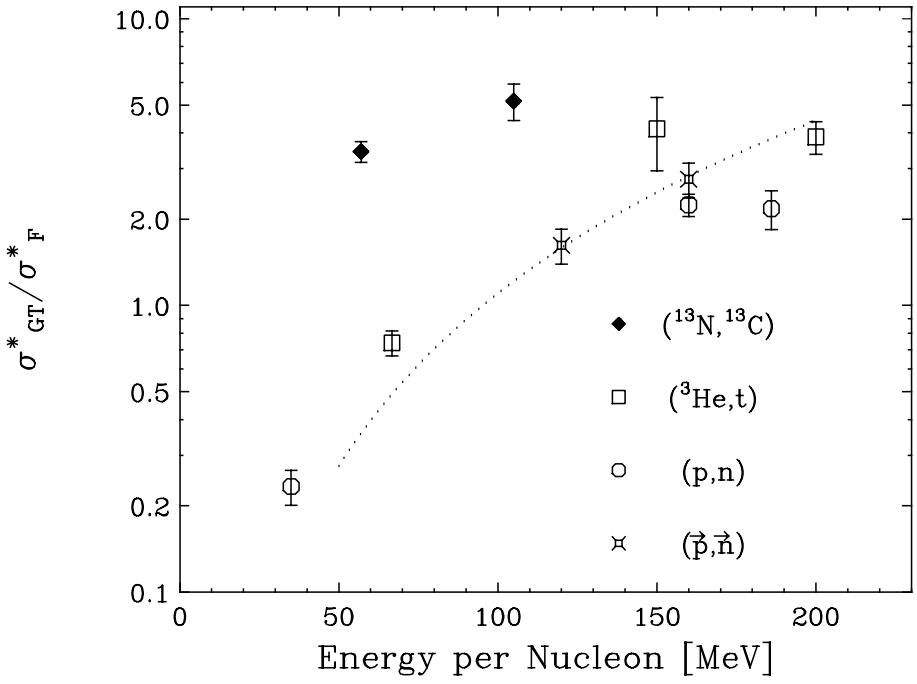

Figure 5.1: Energy dependence of $\sigma^*_{\rm GT}/\sigma^*_F$ for a number of charge–exchange reactions performed on ^{13}C targets. The dotted line is the equivalent of the $\hat{\sigma}_{\rm GT}/\hat{\sigma}_{\rm F} = ({\rm E_p}/55\,{\rm MeV})^2$ curve, scaled appropriately.

Chapter 6

Conclusion and Outlook

With the increasing availability of radioactive nuclear beams, charge–exchange reactions with β–unstable nuclei can now be studied. This is demonstrated by the present work: Quantitative results and high energy resolution were achieved despite a secondary beam with limited intensity and poorly defined momentum.

The difficulties associated with these experiments are obvious. Because of the large emittance of radioactive beams produced by projectile fragmentation, the ion–optical setting of the analyzing beam line has to be tuned much more carefully than for typical primary–beam experiments, since the phase–space volume of the radioactive beam provides a large "lever arm" for image aberrations. Using just the A1200 for production and puricifation of the secondary beam and analysis of the reaction products provides an additional challenge. Further complications are the comparatively low count rate, the limited angular resolution, and the high background rate. A comparison of the quality of the final data of the present work with the results obtained by Raman et al and Ichihara et al (Refs. [AnW91, IcI94]) illustrates the relative difficulty of stable–beam and radioactive–beam experiments.

However, the mirror charge–exchange results are the first of their kind, and major improvements both in beam intensity and in experimental equipment can be

expected at laboratories worldwide. At the NSCL, the coupled–cyclotron upgrade [MSU94] will provide the former, while the S800 spectrograph [Nol89] is the first high–resolution beam–analysis device specifically built for nuclear experiments with radioactive beams. Had the S800 been available as an analysis device for the present study, the A1200 could have been used to produce and purify the secondary beam, and a drastic reduction in background rate could have been realized in addition to improved energy resolution. With a projected energy resolution of $E/\Delta E = 5000$, equivalent to a FWHM of 0.27 MeV for the E/A = 105 MeV experiment, the final ^{13}C resolution would have been 1.9 MeV and thus slightly better than that achieved in the E/A = 57 MeV experiment. At the cost of a reduction in rate, thinner reaction targets could provide excellent overall energy resolution.

The suitability of heavy–ion charge exchange as a tool for weak–interaction strength measurements is another issue addressed by the present work. The analysis of the mirror charge–exchange experiments greatly profits from the symmetry of the mirror system, which aids in the interpretation of the spectra and ensures that only one nuclear form factor enters the picture. In this sense, the mirror reaction offers a unique opportunity for the study of the HICEX process. The present results are compatible with the assumption that the reaction occurs via single–step charge exchange, the underlying physics of which is the nucleon–nucleon interaction. The narrow angular widths of the observed states as well as the good agreement of the shapes of the energy spectra with the shell–model calculations shown in Fig. 4.4 further suggest that the forward cross section is indeed dominated by $\Delta T=1$, $\Delta S=0,1$ (i.e. Fermi and Gamow–Teller) transitions. This is analogous to the results obtained theoretically and experimentally for the (^{6}Li,^{6}He) and (^{12}C,^{12}N) systems, and is another piece of evidence that HICEX can be instrumental in measuring weak–interaction strengths in radioactive nuclei.

Qualitatively, the ^{13}C(^{13}N,^{13}C)^{13}N excitation spectra are readily interpreted in terms of the transitions in projectile and target. The quantitative argument for "specific proportionality" is not quite as strong. While the observed spectra do suggest that the measured cross section is very likely proportional to the strengths of the Fermi and GT transitions, the controversy regarding the interpretation of the 13C(p,n) results renders the conclusions somewhat tentative. Including these uncertainties, it can be said that specific proportionality is born out by the ^{13}C(^{13}N,^{13}C)^{13}N results to within 30–50%.

Clearly, more work remains to be done before HICEX will be as well understood as the (p,n) reaction. From an experimentalist's point of view, it would seem desirable to obtain as much data as possible. The (^{3}He,t) reaction is of interest as a first step towards nucleon–induced charge exchange, while it does not allow angular–momentum transfer to the projectile. It is desirable that CEX reactions should be studied over a wide range of projectiles and targets. Nuclei such as ^{14}C, which has been studied extensively with the (p,n) reaction, as well as other "benign" nuclei should be used as benchmarks to probe the CEX response in a variety of systems.

Mirror charge exchange will also be a valuable tool due to its relative structural simplicity. Two obvious candidates for further mirror HICEX studies are the (^{11}C,^{11}B) and (^{27}Si,^{27}Al) systems. A charge–exchange experiment using the latter has been proposed and has received approval for a feasibility study with the S800 spectrograph [Ste95b]. One of the advantages of the mirror reaction is that it is possible to observe transitions of both Fermi and the Gamow–Teller type. Together with data from the (p,n) and (^{3}He,t) reactions, it is to be hoped that a consistent picture will emerge regarding the relative magnitudes of Fermi and GT unit cross sections. This would greatly aid in calibrating future HICEX results obtained with radioactive beams.

Much work also remains to be done regarding theoretical issues. DWIA calculations, for expample, are very helpful in understanding the general features and trends of the data, such as the effects of energy loss in the reaction. But when absolute cross sections and angular distributions are to be determined, much fine–tuning of model parameters is usually required in order to provide acceptable fits, as shown e.g. in Ref. [RaW87]. While empirical formulae describe most of the (p,n) charge–exchange results rather well, the difficulties associated with the ^{15}N(p,n) and ^{13}C(p,n) results indicate that nucleonic charge exchange is not well enough understood on a microscopic, fundamental level. Until such understanding progresses satisfactorily, theoretical descriptions of HICEX will be at least problematic.

While more work is clearly necessary in both experiment and theory before HICEX reactions can be fully understood, the present results allow cautious optimism. Given the current improvements in beam intensity and spectrometer performance, it can be expected that radioactive nuclear beams will provide the opportunity to reliably measure Gamow–Teller strengths in radioactive nuclei.

Appendix A

The ^{13}C Targets

The targets for the charge–exchange experiments had to satisfy a number of requirements: A thickness of about 10 to 20 mg/cm^2 was required to strike a balance between count rate and and energy resolution. The targets had to be an inch high to cover the target frame, about two inches in width because of the beam size at the dispersive image, and have maximum uniformity so as not to degrade the spectrometer resolution.

Since targets of enriched ^{13}C that meet the above specifications are not offered commercially, they had to be manufactured from available raw materials. First attempts to produce acceptable targets by machine-pressing amorphous ^{13}C powder into pellets were unsuccessful: Even though the pressure applied to the powder was sufficient to leave imprints in the stainless-steel dies, the targets were not self-supporting. A first acceptable batch of targets was produced by dissolving styrofoam in acetone, mixing amorphous ^{13}C powder in and pressing the substance betwe[21 en pieces of glass. After the acetone had evaporated, ^{13}C constituted about half of the targets by weight. A first test run [StB91] showed that a higher target purity was desirable and that a different production method had to be developed.

The targets used in the charge–exchange experiments were made from ^{13}C-labelled

polyethylene [$(^{13}CH_2)_n$, 99% enriched], which was purchased in powder form from the ISOTEC corporation for a price of $3000 for 1 gram. (It may be helpful to know that the procedure outlined here did not work at all with deuterated polyethylene supplied by Cambridge Isotope Laboratories. That material appeared to have a higher melting point than the polyethylene supplied by ISOTEC.)

In order to ensure an even, well–controlled thickness and to avoid air inclusions in the final target, the following procedure was employed in making 10 mg/cm^2 targets:

1. 250 mg of the polyethylene (PE) powder are spread on the clean, polished surface of a steel brick that forms the lower half of a target press and the brick placed in a vacuum oven and heated to 150 degrees C. The powder is left in the oven for a period of around 16 hours, during which it melts and forms small beads on the brick's surface.

2. The oven is then switched off, the vacuum broken, and the brick taken out. Since the brick will retain its temperature for several minutes, a tongue depressor or similar instrument can be used to form the PE into a compact pellet, approximately the size and shape of a large booger.

3. The pellet is again placed on the steel brick, and the brick is placed in the vaccuum oven overnight. Over the course of 24 or so hours, air bubbles inside the plastic will be largely pumped out. What little air remains inside the polyethylene, however, forms large bubbles due to the surrounding vacuum. Therefore, when the oven is switched off, it should also be let up to air, which shrinks the remaining air inclusions to a very small size. When everything has cooled off, the solid pellet of PE is ready for pressing.

4. In order to be able to remove the finished target — which is about 0.1 mm thick

— from the surface of the target press, the polyethylene is sandwiched between two sheets of 2–mil brass shim stock. The brass sheets are first sprayed with a Teflon release agent and then buffed to remove excess material. A practical size for the brass sheets is about three by four inches. Two double–thick strips of shim stock are laid along the length of the sheets as spacers to define the outline of the target and ensure that the material is not pressed thinner than the desired thickness of 0.1 mm (4 mil). The PE pellet is placed on the bottom sheet, the top sheet placed over it, and the target press is assembled and tightened, taking care that the spacers are not displaced. Since spring pressure alone is sufficient to produce the target, the springs of the target press should be preloaded but not fully compressed in order to avoid rupturing the target and creating enclosed air volumes.

5. The target press is placed in the vacuum oven again and left for several hours. The press must be under vaccum well before the pellet begins to melt in order to avoid further air inclusions. Once the target has been formed, the vacuum should be broken and the oven switched off. The press will take an hour or more to cool off by itself, but can also be cooled with water.

The targets produced by this procedure had all desired characteristics. Even though tiny bubbles were visible to the eye, the overall inhomogeneity was better than 10% of thickness, and the deterioration of spectrometer resolution as determined with a beam of ^{13}N at 105 MeV/nucleon was negligible.

Bibliography

[AkD94] H. Akimune, I. Daito, Y. Fujita, M. Fujiwara, M.B. Greenfield, M.N. Harakeh, T. Inomata, J. Jänecke, K. Katori, S. Nakayama, H. Sakai, Y. Sakemi, M. Tanaka, M. Yosoi, Nucl. Phys. **A569**, 234c (1994), *Proceedings of the Gull Lake Nuclear Physics Conference on Giant Resonances, Gull Lake, Michigan, August 1993*, edited by M. Thoennessen (North-Holland 1993).

[AnW91] N. Anantaraman, J.S. Winfield, Sam M. Austin, J.A. Carr, C. Djalali, A. Gillibert, W. Mittig, J.A. Nolen, Jr. and Zhan Wen Long, Phys. Rev. C **44**, 398 (1991).

[AnW61] J.D. Anderson and C. Wong, Phys. Rev. Lett. **7**, 250 (1961).

[AuS93] M.B. Aufderheide, S.D. Bloom, D.A. Resler and G.J. Mathews, Phys. Rev. C. **48**, 1677 (1993).

[Aus94] Sam M. Austin, Paper presented at the International Symposium on Spin–Isospin Responses and Weak Processes in Hadrons and Nuclei, Osaka, Mar. 8–10, Osaka, Japan.

[AuA94] Sam M. Austin, N. Anantaraman, W.G. Love, Phys. Rev. Lett. **73**, 30 (1994).

[BeE87] G.F. Bertsch, H. Esbensen, Rep. Prog. Phys. **50** (1987) 607.

[Ber93] C.A. Bertulani, Nucl. Phys. **A554**, 493 (1993).

[BrR77] K.L. Brown, F. Rothacker, D.C. Carey, Ch. Iselin, SLAC Report No. 91 (1977)

[Car64] D.C. Carey, National Accelerator Laboratory Report NAL-64.2041 (1964)

[ChB93] W.–T. Chou, B.A. Brown, E.K. Warburton, Phys. Rev. C **47**,163 (1993).

[DoG75] R.R. Doering, A. Galonsky, D.M. Patterson, G.F. Bertsch, Phys. Rev. Lett. **35**, 1961 (1975).

[Gaa85] C. Gaarde, *Nuclear Structure 1985*, R. Broglia, ed., Copenhagen (1985), North–Holland.

[GoG80] C.D. Goodman, C.A. Goudling, M.B. Greenfield, J. Rapaport, D.E. Bainum, C.C. Foster, W.G. Love, F. Petrovich, Phys. Rev. Lett. **44**, 1755 (1980).

[GoB85] C.D. Goodman, R.C. Byrd, I.J. Van Heerden, T.A. Carey, D.J. Horen, J.S. Larsen, C. Gaarde, J. Rapaport, T.P. Welch, E. Sugarbaker, T.N. Taddeucci, Phys. Rev. Lett. **54**, 877 (1985).

[IcI94] T. Ichihara, M. Ishihara, H. Ohnuma, T. Niizeki, Y. Tajima, T. Yamamoto, Y. Fuchi, S. Kubono, M.H. Tanaka, H. Okamura, S. Ishida, S. Miyamoto and H. Toyokawa, Phys. Lett. B **323**, 278 (1994).

[JäB94] J. Jänecke, F.D. Bechetti, A.M. van den Berg, G.P.A. Berg, G. Brouwer, M.B. Greenfield, M.N. Harakeh, M.A. Hofstee, A. Nadasen, D.A. Roberts, R. Sawafta, J.M. Schippers, E.J. Stephenson, D.P. Stewart and S.Y. van der Werf, Nucl. Phys. **A526**, 1 (1991).

[LeK80] T.–S. H. Lee and D. Kurath, Phys. Rev. C **21**,293 (1980).

[LeW89] H. Lenske, H.H. Wolter, H.G. Bohlen, Phys. Rev. Lett. **62**, 1457 (1989).

[LeA94] M.Lewitowicz, R.Anne, G.Auger, D.Bazin, C.Borcea, V.Borrel, J.M.Corre, T.Dorfler, A.Fomichov, R.Grzywacz, D.Guillemaud-Mueller, R.Hue, M.Huyse, Z.Janas, H.Keller, S.Lukyanov, A.C.Mueller, Yu.Penionzhkevich, M.Pfützner, F.Pougheon, K.Rykaczewski, M.G.Saint-Laurent, K.Schmidt, W.D.Schmidt-Ott, O.Sorlin, J.Szerypo, O.Tarasov, J.Wauters, J.Zylicz, Phys. Lett. B **332**, 20 (1994)

[MiA91] J.L. Mildenberger, W.P. Alford, A. Celler, A. Häusser, K.P. Jackson, B. Larson, B. Pointon, A. Trudel, M.C. Vetterli, S. Yen, Phys. Rev. C **43**,1777 (1991).

[MSU94] *The $K500 \otimes K1200$, A Coupled Cyclotron Facility at the National Superconducting Cyclotron Laboratory, Michigan State University* MSUCL-939, July 1994

[Nol89] J.A. Nolan, Jr., A.F. Zeller, B.M. Sherrill, J.C. DeKamp, J. Yurkon, *A proposal for construction of the S800 spectrograph*, MSU Report MSUCL-694, July 1989.

[OsA92] F. Osterfeld, N. Anantaraman, Sam M. Austin, J.A. Carr, J.S. Winfield, Phys. Rev. C **45**, 2854 (1992).

[RaW87] J. Rapaport, D. Wang, J.A. Carr, F. Petrovich, C.C. Foster, C.D. Goodman, C. Gaarde, J. Larsen, C.A. Goulding, T.N. Taddeucci, D. Horen, E. Sugarbaker, Phys. Rev. C **36**, 500 (1987).

[RaS95] J. Rapaport and E. Sugarbaker, Annu. Rev. Nucl. Part. Sci. 1994. 44:109-153.

[Rap95] J. Rapaport, private communication.

[Rii94] K. Riisager, Rev. Mod. Phys. **66**, 1105 (1994).

[ScF94] R. Schneider, J. Friese, J. Reinhold, K. Zeitelhack, T. Faestermann, R. Gernhauser, H. Gilg, F. Heine, J. Homolka, P. Kienle, H.J. Körner, H. Geissel;, G.M. Münzenberg, K. Sümmerer, Z. Phys. A **348**, 241 (1994).

[dSF74] A. deShalit, H. Feshbach, Theoretical Nuclear Physics Volume I, Wiley Interscience 1991.

[ShM91] B.M. Sherrill, D.J. Morrissey, J.A. Nolen, Jr., J.A. Winger, Nucl. Instr. Methods **B56**, 1106 (1991).

[She95] B.M. Sherrill, private communication

[StB91] M. Steiner, W. Benenson, C. Bertulani, E. Kashy, R.A. Kryger, N.A. Orr, B.M. Sherrill, M. Thoennessen, S.J. Yennello, B.M. Young, NSCL Annual Report 1991.

[Ste95] M. Steiner, Sam M. Austin, D. Bazin, W. Benenson, C.A. Bertulani, J.A. Brown, M. Fauerbach, M. Hellström, E. Kashy, J.H. Kelley, R.A. Kryger, T. Kubo, N.A. Orr, R. Pfaff, B.M. Sherrill, M. Thoennessen, S.J. Yennello, B.M. Young, P.D. Zecher, D.J. Morrissey, C.F. Powell, subm. to Phys. Rev. Lett.

[Ste95b] M. Steiner etc., NSCL Proposal (PAC 16), July 1995.

[TaG87] T.N. Taddeucci, C.A. Goulding, T.A. Carey, R.C. Byrd, C.D. Goodman, C. Gaarde, J. Larsen, D. Horen, J. Rapaport, E. Sugarbaker, Nucl. Phys. **A469**, 125 (1987).

[WaP85] J.W. Watson, W. Pairsuwan, B.D. Anderson, A.R. Baldwin, B.S. Flanders, R. Madey, R.J. McCarthy, B.A. Brown, B.H. Wildenthal, C.C. Foster, Phys. Rev. Lett. **55**, 1369 (1985).

[Wat94] J.W. Watson, private communication.

[WiA86] J.S. Winfield, N. Anantaraman, Sam. M. Austin, L.H. Harwood, J. van der Plicht, H.–L. Wu, A.F. Zeller, Phys. Rev. C **33**, 1333 (1987).

[WiA87] J.S. Winfield, N. Anantaraman, Sam M. Austin, Ziping Chen, A. Galonsky, J. van der Plicht, H.-L. Wu, C.C. Chang and G. Ciangaru, Phys. Rev. C **35**, 1734 (1987).

[Wol87] H. Wollnik, The Optics of Charged Particles, 1978.